In situ synchrotron study of sintering of gas-atomized Ti-6Al-4 V powders using concomitant micro-tomography and X-ray diffraction: Effect of particle size and interstitials on densification and phase transformation kinetics

M. Pontoreau, M. Coffigniez, V. Trillaud, Christophe Le Bourlot, J. Lachambre, Laurent Gremillard, M. Perez, E Maire, J. Adrien, P. Steyer, et al.

To cite this version:

M. Pontoreau, M. Coffigniez, V. Trillaud, Christophe Le Bourlot, J. Lachambre, et al.. In situ synchrotron study of sintering of gas-atomized Ti-6Al-4 V powders using concomitant micro-tomography and X-ray diffraction: Effect of particle size and interstitials on densification and phase transformation kinetics. Acta Materialia, 2023, 246, pp.118723. 10.1016/j.actamat.2023.118723 . hal-04018206

HAL Id: hal-04018206
https://hal.science/hal-04018206

Submitted on 13 Mar 2023

Full length article

In situ synchrotron study of sintering of gas-atomized Ti-6Al-4 V powders using concomitant micro-tomography and X-ray diffraction: Effect of particle size and interstitials on densification and phase transformation kinetics

M. Pontoreau [a], M. Coffigniez [a], V. Trillaud [a], C. Le Bourlot [a], J. Lachambre [a], L. Gremillard [a], M. Perez [a], E. Maire [a], J. Adrien [a], P. Steyer [a], T. Douillard [a], A. King [b], X. Boulnat [a,*]

[a] *INSA Lyon, University of Lyon, MATEIS, UMR CNRS 5510, F69621 Villeurbanne, France*
[b] *Synchrotron Soleil, Psiché Beamline, F-91190 Gif-sur-Yvette, France*

ARTICLE INFO

Keywords:
Titanium alloy
Synchrotron micro-tomography
X-ray diffraction
Additive manufacturing
Sintering

ABSTRACT

Compared to the well-established powder bed fusion techniques, sinter-based additive manufacturing of titanium alloys remains extremely challenging. This technique involves three steps: (i) shaping of a part composed of metallic powders bound with polymeric binder (ii) debinding (iii) sintering. One main issue is that densification during the solid sintering is promoted by small powder particles whereas the latter have a high propensity to carbon and oxygen uptakes from the binder, which are detrimental to ductility of titanium parts. In this article, we report a unique in-depth characterization of solid sintering of titanium powders using *in situ* coupled micro-computed tomography (μCT) and X-Ray diffraction under synchrotron radiation at high temperature, combined with *in situ* environmental scanning electron microscopy (HT-eSEM). Evolution of global porosity, pore size distribution and interconnectivity as well as allotropic titanium phase transformation and precipitation of second-phase precipitates (titanium carbides) were determined, allowing a discussion on the densification/phase transformation relationship. This multi-scale *in situ* study of solid sintering was used to identify the effect of powder particle size on the contamination / densification trade-off. Carbon/oxygen uptakes clearly increase the α-to-β transus but do not affect significantly the final porosity of the sintered parts, which argues for a secondary role of the β phase on the sintering kinetics of titanium alloys. Reducing the powder particle size has a tremendous effect on both the densification kinetics and the final pores structure.

1. Introduction

Metal additive manufacturing now has many industrial applications and is attracting worldwide scientific and technological interest. In particular, the healthcare sector has been a pioneer in the 3D printing of orthopedic and dental implants, whose leading alloy is titanium [1]. Its mechanical strength, fatigue life, corrosion and biological properties make it a reference material for the industrial sector. However, the intrinsic favourable properties of the material can be undermined by additive manufacturing processes. Hence, numerous studies were performed to tackle this issue and enhance the quality of printed parts [2–3]. In powder bed fusion, by laser (L-PBF) or electron beam (EB-PBF), defects are indeed increasingly controlled, although surface integrity remains a major challenge, particularly for cyclic properties. Residual stresses in the Ti-6Al-4 V alloy from L-PBF are also an obstacle to the production of solid (large) parts and require stress relief treatment [4]. A promising alternative is sintering-assisted additive manufacturing: direct-ink writing (DIW) [5–7], Fused Filament Fabrication (FFF) [8] or metal binder jetting (MBJ) [9,10]. These processes have the advantage of not going through melting and therefore limit the occurrence of residual stresses while maintaining a microstructure closer to equilibrium. Compared to PBF techniques, sinter-based AM (SBAM) methods enable to produce metallic parts presenting both closed and open pores forming interconnected networks, with characteristic pore sizes between the micron and the millimeter. In the case of biocompatible metallic alloys such as Ti-6Al-4 V, such porous-controlled structures are considered

---

[*] Corresponding author.
E-mail address: xavier.boulnat@insa-lyon.fr (X. Boulnat).

very interesting for applications in contact with bones [11–13] because it can favor vascularization (macropore network) [14] and bone ingrowth (micropore network) [15,16].

However, the production of Ti-6Al-4 V parts by SBAM with the desired porosity combined with high mechanical properties, requires a perfect control of both debinding and sintering thermal treatments [12]. On the one hand, the debinding step of the printed green parts should lead to a complete elimination of the organic phase, used for the formulation of the powder-based ink, without inducing excessive pollution of the metallic particles by diffusion of interstitials such as carbon, hydrogen and oxygen atoms. Such residual atoms would affect the subsequent sintering and the final properties of the materials (embrittlement [17]), which often prevents the designed part from matching the requirements of the ASTM F1108 standard and/or ISO 5832–3 suitable for bone implant applications. On the other hand, the sintering step shall be designed to reach both optimized mechanical properties and porosity for a given composition. This diffusion-driven process is generally performed in the solid state for titanium, whereas supersolidus liquid sintering is sometimes carried out for certain categories of alloys, particularly steels [18]. However, the specificity of the binder/powder systems in SBAM processes implies a detailed understanding of the relationships between initial powders, debinding parameters (and therefore possible inorganic residue content) and sintering kinetics. These parameters play a major role in the mechanical and functional behavior of the parts, since the microstructure, chemical composition, porosity and therefore the properties of the printed parts are determined here.

Debinding/sintering of titanium alloy powders have been studied in the framework of the Metal Injection Molding process (MIM) [18–20]. This process differs from SBAM processes regarding both the powder size distribution and the binder used for shaping. More recently, previous work dedicated to the comprehension and optimization of the debinding step of Ti-6Al-4 V printed by DIW [21] has demonstrated that lowering the debinding temperature permits to significantly reduce C and O uptake by hindering diffusion of such interstitial elements in Ti-6Al-4 V particles. Compared to other debinding procedure at higher temperatures [22–25], this debinding step could prevent the precipitation of carbides in the scaffolds sintered.

Even more importantly, the sintering behavior of printed parts needs to be more deeply studied in order to fully control the evolution of the pores shape, size, location and interconnectivity in the material. Numerous studies have already highlighted the effect of different sintering parameters on the densification of titanium alloys. Concerning the atmosphere for instance, vacuum sintering has to be preferred. Indeed oxygen-poor atmospheres prevent oxidation of the alloy [26]. Besides, compared to sintering in argon, vacuum sintering enables a better removal of volatile pollutants like hydrogen [27]. The effect of the powder size is often studied as smaller particles lead to higher final densification by modifying the specific surface area [28–30]. More specifically, the temperature and holding times of the sintering heat treatment must be defined for a targeted densification. Even if densification may already occur at 900 °C as suggested by Xu et al., compacts are typically densified above 1300 °C to reach a density above 95% of the theoretical density [30–31]. Using DIW, Elsayed et al. reached densities above 97% in printed parts by sintering Ti-6Al-4 V powder having a mean diameter (d_{50v}) of 10 μm at 1450 °C for 2 h [24]. Most studies about sintering of Ti-6Al-4 V are based on the final characterization of the sintered materials using Archimedes' principle, pycnometry and/or scanning electron microscopy (SEM) characterization [24,29,33–35]. For 3D characterization, X-Ray micro-tomography (μCT) is a powerful *ex situ* analytical tool which gives quantitative information on the porosity (shape, size, volume fraction of interconnected and closed pores, …) [12,36,37]. These *ex situ* measurements can be coupled with *in situ* dilatometry in order to assess the densification kinetics of the initial pellets [28,32,38]. Nevertheless, such an *ex situ* approach does not allow to describe the time/temperature evolution of the pores size and morphology throughout the sintering treatment. It appears that *in situ* X-Ray microtomography would be perfectly adapted as a non-destructive analysis of the internal structure of the material. Few years ago, Lame *et al*. presented, for the first-time, an *in situ* X-Ray synchrotron microtomography (S-μCT) study focused on the sintering of copper and steel powders [39,40]. Then, S-μCT was further used to characterize *in situ* the heat treatment of either ceramic powders [41], metallic powders [42] or bulk metallic alloys [43]. These studies clearly gave great insight into the densification behavior of powders and how S-μCT can be used. However, in the framework of SBAM processes of titanium parts, key scientific questions remain: how does the binder residues influence phase transformation of allotropic (such as titanium alloy) metallic system? How does it interact with the densification kinetics? How does the particle size distribution, thus specific surface areas, contribute to the trade-off between densification *versus* contamination by interstitial elements? With them, challenging experimental investigations shall be carried out because the evolution of the pore architecture must be followed *in situ* concomitantly with the phase transformation. The allotropic α-β phase transformations (around 900 °C) can be recorded by conventional X-Ray diffraction (XRD) [44–46], or through a more dynamic approach, using the synchrotron (S-XRD). S-XRD has already been used to characterize titanium alloys phase transformations during either a heat treatment [47–50] or under mechanical stress [51].

Here, we led a unique study by coupling S-μCT and S-XRD in order to describe not only the evolution of the porosity but also the phase transformations during sintering of two different Ti-6Al-4 V powders. Firstly, the evolution of the porosity will be studied during the sintering, with regards to the powder size and pollution (interstitials content) induced by the debinding step. Secondly, *in situ* S-XRD measurements will permit to determine the α→β phase transformations kinetics as well as variations of the cell parameters during thermal treatment. These variations will be related to the chemical composition of phases and, consequently, to the amount of interstitial elements in the different debinded powders. Finally, correlations between densification and phase transformation will be discussed in light of a complementary *in situ* local characterization by high-temperature SEM. We describe how two sintering parameters (time and temperature) can be used to tailor porosity and microstructure of titanium parts produced by sinter-based additive manufacturing processes.

2. Experimental procedure

2.1. Materials: as-atomized and debinded powders

Two different batches of Ti-6Al-4 V gas-atomized powders were purchased from TLS Technik GmbH (Germany): Ti36 (d_{90v} about 36 μm), which has a powder size distribution close to that used in L-PBF, and Ti6 (d_{90v} about 6 μm), which is much finer. Their chemical composition is given in Table 1. Particle size distributions of the spherical powders were measured with a laser granulometer (Mastersizer 2000, Malvern Instruments Ltd, UK) as follows: $d_{10v} = 2.93 \pm 0.02$ μm; $d_{50v} = 4.31 \pm 0.07$ μm; $d_{90v} = 5.83 \pm 0.07$ μm for the “Ti6” powder, and $d_{10v} = 11.6 \pm 0.2$ μm; $d_{50v} = 23.1 \pm 0.1$ μm; $d_{90v} = 37.2 \pm 0.4$ μm for the “Ti36” powder. More information on the powder size distribution can be found in a previous study (see Fig. 1 in [52]).

To simulate interstitials contamination of 3D printed parts after debinding, these powders were shaped as scaffolds by DIW following the procedure already detailed in previous works [12,21]. To summarize, Pluronic F127 (triblock co-polymer surfactant purchased from Sigma Aldrich) was used to form a hydrogel (25 wt% Pluronic F-127 in water) loaded with 50 vol% of Ti-6Al-4 V. Then, scaffolds were printed by the extrusion of the ink using a robocaster (3D Inks, LLC, Stillwater, OK, USA) controlled by the Aerotech A3200 motion software (Aerotech Inc., Pittsburgh, PA, USA). For this study, dried scaffolds (48 h at 25 °C) were thermally debinded using a Nabertherm N 11/hr furnace, under primary

Table 1
Compositions (wt%) of the Ti-6Al-4 V as-atomized (supplier values) and debinded powders (*NM* = not measured).

	Chemical element	Ti	N	C	O	H	Fe	Al	V
As-atomized (supplier)	Ti36 powder	Bal.	0.005	0.01	0.08	<0.001	0.22	6.20	3.98
	Ti6 powder	Bal.	0.008	0.011	0.15	0.002	0.155	6.10	3.87
Debinded (measured)	Ti36_DB350	Bal.	*NM*	0.130	0.125	*NM*	*NM*	*NM*	*NM*
	Ti36_DB500	Bal.	*NM*	0.187	0.335	*NM*	*NM*	*NM*	*NM*
	Ti6_DB350	Bal.	*NM*	0.106	0.745	*NM*	*NM*	*NM*	*NM*

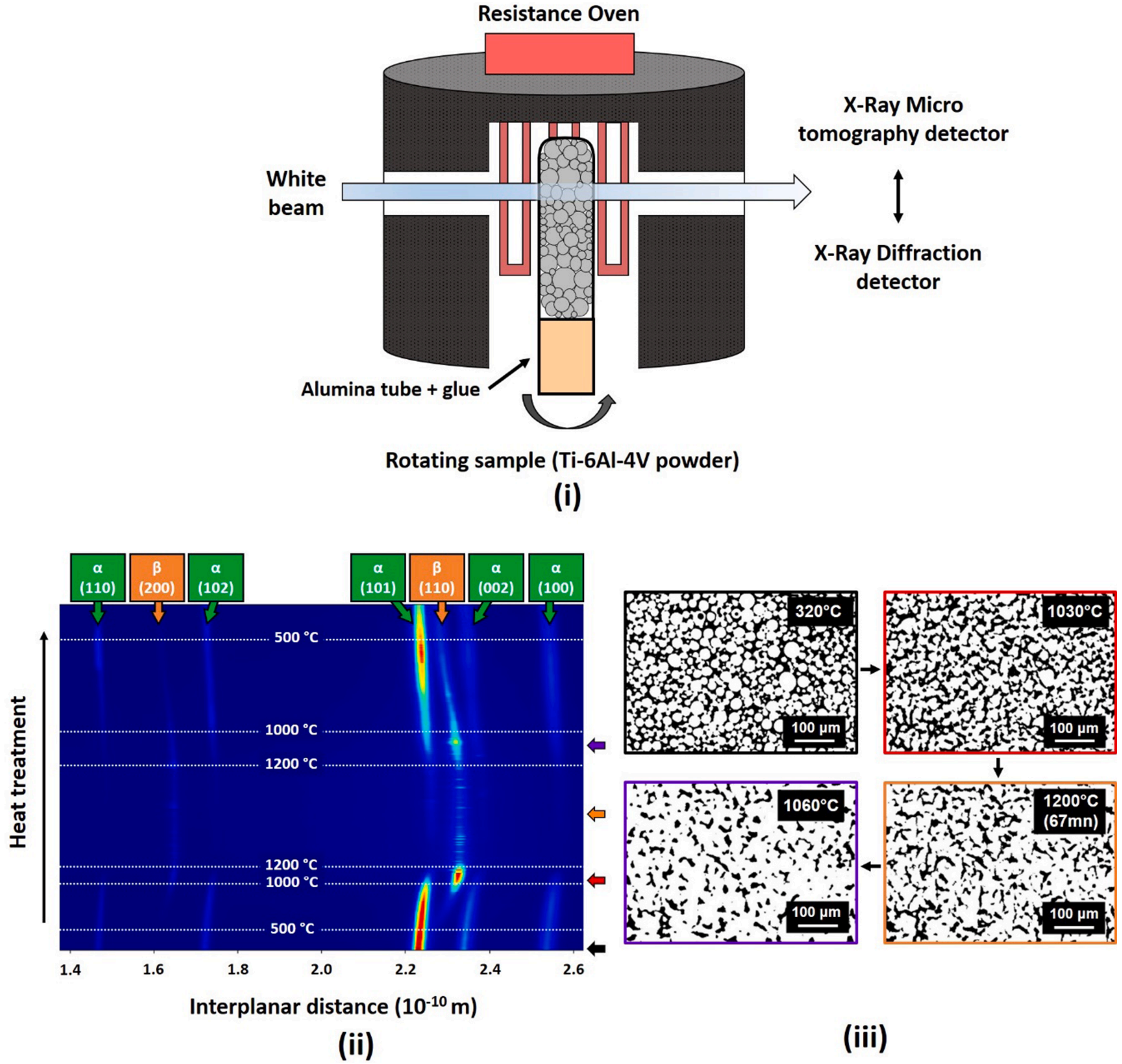

Fig. 1. (i) Representation of beamline setup and typical data collected for sample Ti36_DB500 during the whole heat treatment: (ii) color map displaying the evolution of the S-XRD peak intensities and positions of both α- and β-phases for one detector and (iii) binarized slices of S-µCT analyzed volumes at specific times and temperatures.

dynamic vacuum (around 5×10^{-2} mbar) and using two different sets of conditions: either 30 min at 350 °C (1 K/min), referred to “Ti36_DB350” or “Ti6_DB350” or 2 h at 500 °C (1 K/min), referred to “Ti36_DB500”. The debinded scaffolds were then gently crushed to recover the powder that was further used for the investigations. C and O contents measured by the infrared combustion methods in the as-received and the debinded states illustrate the prime role of debinding on the C and O uptakes (see Table 1).

2.2. In situ synchrotron experimental setup

2.2.1. Description of samples, furnace and coupled S-XRD/S-μCT

Synchrotron experiments were carried out using the PSICHE beamline at the SOLEIL synchrotron (Gif-sur-Yvette, France). The experimental setup (see Fig. 1) was composed of a resistance furnace in which samples were mounted on a 360° rotating stage. The samples were heated at 10 K/min from 20 °C to 1200 °C, held 2 h at 1200 °C, then cooled at 5 K/min, slowly enough to avoid the martensitic transformation upon cooling. Acquisition of data was typically stopped below 500 °C during the cooling step, for saving synchrotron beam time. The powders were encapsulated in quartz tubes (inner diameter = 1 mm, outer diameter = 3 mm) under primary vacuum (5×10^{-2} mbar after 3 argon purges). The quartz tubes were fixed onto hollow alumina tubes with a high-temperature glue.

2.2.2. Coupling in situ synchrotron XRD/μCT measurements

In order to couple S-XRD with S-μCT, the use of a pink beam (30–80 keV) was chosen because it allows to get both energy dispersive S-XRD and high-flux S-μCT. Indeed, this solution enables fast acquisition with short switch time between tomography and the diffraction configuration, which seems more suitable to characterize a moderately fast dynamic process such as sintering. Typically, during heat treatment, S-XRD data were acquired continuously between S-μCT analyses which were carried out every 10 min.

S-μCT measurements and data processing: a set of 1200 2D projections along a 180° sample rotation with 5 ms of exposure per projection was acquired for each S-μCT scan. The tomographic volumes of $1330 \times 1330 \times 665$ μm^3 were, thus, acquired with a scan duration of 6 s and with an isotropic voxel size of 0.65 μm. 3D volumes (32 bits) were reconstructed from 2D projections using PyHST2 software [53]. The exposure time had to be minimized so that local variations of the microstructure during collection time did not induce significant data alteration. The quality of sample centering and sample fixation influences the quality of the data acquired as well. It should also be noted that the voxel size was chosen to enable the characterization of the evolution of the porosity in the coarse powder samples. For fine powder sample, preliminary experiments showed that the voxel size should be sufficient to observe the initial porosity in the granular stack. However, the spatial resolution would not permit to properly describe pores below a certain size which is mentioned hereafter.

For the analysis of the 3D volumes, the files were converted in 16 bits and analysed volumes of $665 \times 665 \times 665$ μm^3 were extracted from the total volume in order to consider only the granular stack composed of matter (the powders) and porosity. In other words, voids outside the granular stack were not considered. Image processing and analysis of the reconstructed volume were performed with the Fiji software [54]. First, a 3D bilateral filtering of the volumes was applied (spatial sigma = 2 voxels, radius = 6 voxels, gray sigma = 2000 for 16-bit grayscale) in order to reduce the noise in the image and to facilitate the segmentation process at the expense of a slight resolution loss.

The determination of the threshold to differentiate between matter and void is critical. Based on the 16-bit histograms, the Isodata algorithm gives a satisfactory result only if there is no significant movement inside the tubes and so if the quality of the scans is maximum. For a given sample, the Isodata algorithm [55] was successfully used for the first and last scan and it permits to determine the initial and final porosity of the studied samples with a very good accuracy. For the intermediate scans of a lesser quality, it has been chosen to determine the threshold knowing the initial and final porosity determined using the Isodata algorithm. The evolution of the porosity can be plotted from the evolution of the mean grayscale per voxel which is related to the evolution of the amount of Ti-6Al-4 V inside the rectangular cropped scans. Consequently, the threshold to apply are determined in accordance with this evolution (see Supplementary Materials for more details). Despite some discontinuities in the results (see Section 3), the thresholds determined effectively differentiate between matter and void in these intermediate low quality scans.

After binarization, the different pores were labelled (one label per pore) to get dimensional information on each of them. The definition of a pore here is then a cluster of connected voxels (touching either at faces, edges or vertices). Pores composed of less than nine voxels were not kept for characterization because they are considered as noise. Consequently, this arbitrary choice defines the minimum size of the pores analyzed as equal to 2.47 μm^3 (equivalent diameter of 1.68 μm). The smaller clusters are disregarded from the analysis because they can easily be confused with noise, inherently present in any X Ray tomography reconstruction. We believe that the small size and quantity of these pores is so small that omitting them has a minor effect on our results. The interpretation of the dimensional data collected will permit to describe precisely the evolution of the interconnected porosity initially present in the granular stack and of the closed pores forming during the heat treatment.

In order to properly describe the geometrical evolutions of the solid phase (the particles skeleton, not the pores), the plugin "Local Thickness" was used in the Fiji software [56]. This plugin enables to assess the thickness of objects contained in a 3D volume by filling the objects with spheres. For each point, this plugin gives the largest sphere that fits inside a phase and contains the point. Then, the plugin attributes to each point a value representing the diameter of this sphere (see Supplementary Materials). This method is particularly appropriate in the case of Ti particles and of interconnected porosity, *i.e.* when clusters of voxels touch each other.

S-XRD measurements and data processing: using a 30–80 keV pink beam, four XRD detectors were placed at angular positions between 8.072° and 8.327° (d-spacing between 1.11 and 2.97 Å), which included the main diffraction peaks of the expected phases. For each measurement, the signal was integrated for 15 s over a 180° rotation of the sample. The S-XRD patterns were recorded continuously between each S- μCT analysis and directly converted into d-spacing based on previous PSICHE beamline calibration (see Fig. 1). The data collected on the four channels were firstly independently analysed. Using Lmfit Python Library [57], a fitting procedure was set up which consists in fitting the background with a linear function and each peak with pseudo-Voigt function. For each fit, reduced chi-square parameter for whole spectra was saved as well as integrated intensity (area), position, width at half-maximum and the relative fraction of the Gaussian and Lorentzian components of each peak. Then, for each channel, the 5% of the worst fits were removed regarding the reduced chi-square parameter. Due to the small size of the analysed volume, the integrated intensity of a given peak in the S-XRD pattern can dramatically increase when a non-common large grain is in Bragg condition. In order to detect these “overshoots”, the information of a peak for a given channel was filtered if the integrated intensity of this peak was outside of the interquartile (13–87%) computed for this given peak considering all channels. Finally, the average of integrated intensity, position, width at half-maximum and fraction of each peak were computed to average the information collected on the different channels.

In order to estimate the respective evolution of the different phases, the integrated intensity of the peaks was used to compute the area fraction of each phase (α-, β- or even TiC phases) (see (Eq. (1)). For this study, only this semi quantitative estimation was considered. A dedicated calibration with the phases studied would have been necessary for a more fully quantitative Rietveld analysis.

$$\textit{Area fraction of phase } i = \frac{\sum \textit{Integrated intensity of peaks of phase } i}{\sum \textit{Integrated intensity of all peaks}} \tag{Eq. 1}$$

The evolution of the cell parameters was computed considering the interplanar distance evolution of the most intense peaks of each phase. For the hcp α phase, the cell parameters *a* and *c* have been computed using the peaks (110) and (002) respectively. For the bcc β phase, the cell parameter *a* has been deduced from both (200) and (110) peaks. The average lattice parameter of α- and β-phases have been computed as follows:

$$L_{average,\alpha} = \sqrt[3]{a^2 c \ \sin(120^\circ)} \qquad \text{(Eq. 2)}$$

$$L_{average,\beta} = a \qquad \text{(Eq. 3)}$$

2.3. *In situ HT-eSEM analysis of as-atomized powders*

In addition to the synchrotron experiments, the same as-atomized powders were also analysed at high temperature using an Environmental SEM Thermo Fisher Scientific Quattro S. The *in situ* characterization of the powders during the thermal treatment focused on aggregates composed of 6 to 8 particles in contact. Two specific areas were particularly observed: the whole aggregate, to have an overview of the heat-induced phenomena, and the contact area between particles where the sintering may initiate. The 2D aggregates were obtained by drying an ethanol solution in which the powder was dispersed on a thin alumina plate (0.15 mm thickness). Using a 1400 °C heating stage, heat treatments similar to those described earlier were reproduced at a N_2 pressure of 15×10^{-2} mbar. For all experiments, characterization started from 400 °C during the heating ramp (10 K/min) and stopped during the cooling ramp (5 K/min) at 600 °C. Compared to S-μCT, the better resolution of SEM would enable to follow local sintering mechanisms, such as the formation and growth of interparticular necks during sintering. To a certain extent, HT-eSEM was used as a small-scale characterization method, possibly completing and validating the global kinetics evidenced by the *in situ* synchrotron XRD/μCT approach.

To conclude the “Experimental Procedure” part, the Table 2 summarizes the purpose of each *in situ* characterization technique used for the study of the sintering of Ti-6Al-4 V particles. In the following parts, the results will be presented independently for each characterization technique before being discussed all together in the Discussion part.

3. Results

3.1. *Sintering kinetics by in situ S-μCT*

3.1.1. *Global evolution of porosity during sintering*

Fig. 2 shows the evolution of the volume fraction of all pores combined during heat treatment for the different samples. For all samples, the porosity values computed before and after sintering are in accordance with *ex situ* μCT measurements reported in Coffigniez’s PhD thesis [58], which validates the data processing. For coarse powder samples, the porosity significantly dropped from 1000 °C, continued to decrease during all the holding step and stabilized below 850 °C during the cooling step. The differences between all coarse powder samples will be further discussed later. By averaging the three coarse powder samples, the final porosity of the sintered materials was equal to 13.2 ± 1.6 vol%. Unless otherwise stated, the values given for the coarse powder samples will, from now on, be averages calculated over the three samples. As expected, the densification of Ti6_DB350 not only starts at lower temperature but is almost completed (0.5 ± 0.3 vol% of detectable pores) before the holding step starts.

Table 2
Relation between the *in situ* characterization techniques involved and the phenomena studied during the sintering of Ti-6Al-4 V particles.

Characterization technique	Phenomena/Effects studied
***In situ* X-Ray μCT (synchrotron)**	- Evolution of geometrical characteristics of the solid phase and of the porosity (interconnected pore and closed pores) - Densification kinetics: effect of powder size and residual contents
***In situ* X-Ray Diffraction (synchrotron)**	- α-β transformation: phase fraction and lattice parameter - Detection of titanium carbide depending on C content
***In situ* high temperature environmental SEM (laboratory)**	- Formation and growth of interparticular necks between particles, including between fine particles Ti6 that cannot be observed with μCT

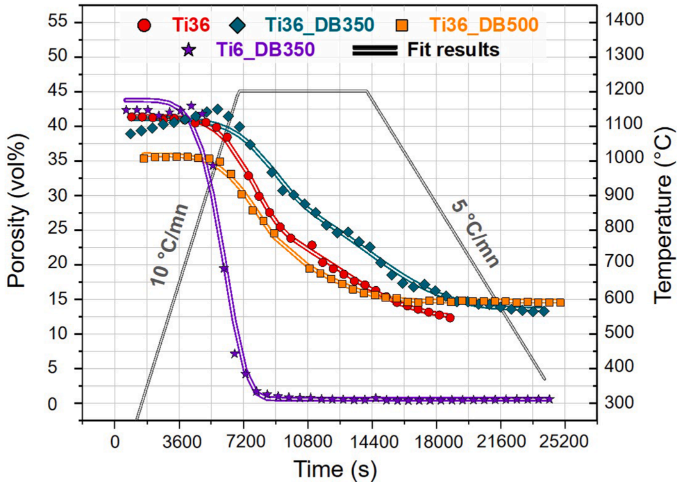

Fig. 2. Difference between the samples in the evolution of the pore volume fraction during the heat treatment: partial densification of coarse powder samples and complete densification of fine powder sample. Fit results are discussed in Section 4.1.

For coarse powder samples, final densities are quite similar from one sample to another, which suggests that the presence of residues after the debinding step (higher C and O contents compared to pristine powder, see Table 1) does not significantly prevent the sintering of Ti-6Al-4 V particles. Indeed, presence of residues could have a significant impact on the sintering progress by oxidation or carbide precipitation at the surface of Ti particles. Regarding titanium alloys, it was reported that the initial oxide layer does not alter sintering as the layer may be resorbed by diffusion of oxygen into the bulk above 550 °C [27]. At high temperature, the oxide layer may also partially crack due to the mismatch of thermal expansion coefficients between the oxide layer and the Ti-6Al-4 V. Thus, additional C and O atoms likely diffuse into the particles during the sintering treatment instead of preventing diffusion between particles. Nevertheless, it is worth mentioning that the final densities of the coarse powder samples are in line with the measured amount of residue (see Table 1): the higher the amount of residue (Ti36_DB500 > Ti36_DB350 > Ti36), the higher the final porosity (14.7 ± 0.1 > 13.5 ± 0.5 > 12.2 ± 0.6 vol%, respectively). Therefore, the amount of residue could still have a slight impact on the densification. These slight differences should be further investigated in the light of more experiments and, consequently, more statistically significant results. Nevertheless, the main conclusion here remains that the residual C and O contents are of second order compared to the powder size for the densification kinetics in this study.

3.1.2. *Analysis of individual pores and solid phase in Ti36 samples*

The evolution of both the morphology of the solid phase (particles and further sintering necks) and the porosity were studied in more details for coarse powder samples. It is worth mentioning that such a detailed study was not possible for the Ti6_DB350 sample, whose pores are too small.

Fig. 3 shows the evolution of the characteristic thicknesses of the solid phase measured by “Local Thickness” plugin (gives the largest sphere that fits inside the particle). The label q50 represents the median thickness in volume and the other labels represent different percentiles of the distribution. 2D and 3D representations of the size distribution deduced from the Local Thickness plugin are shown for sample

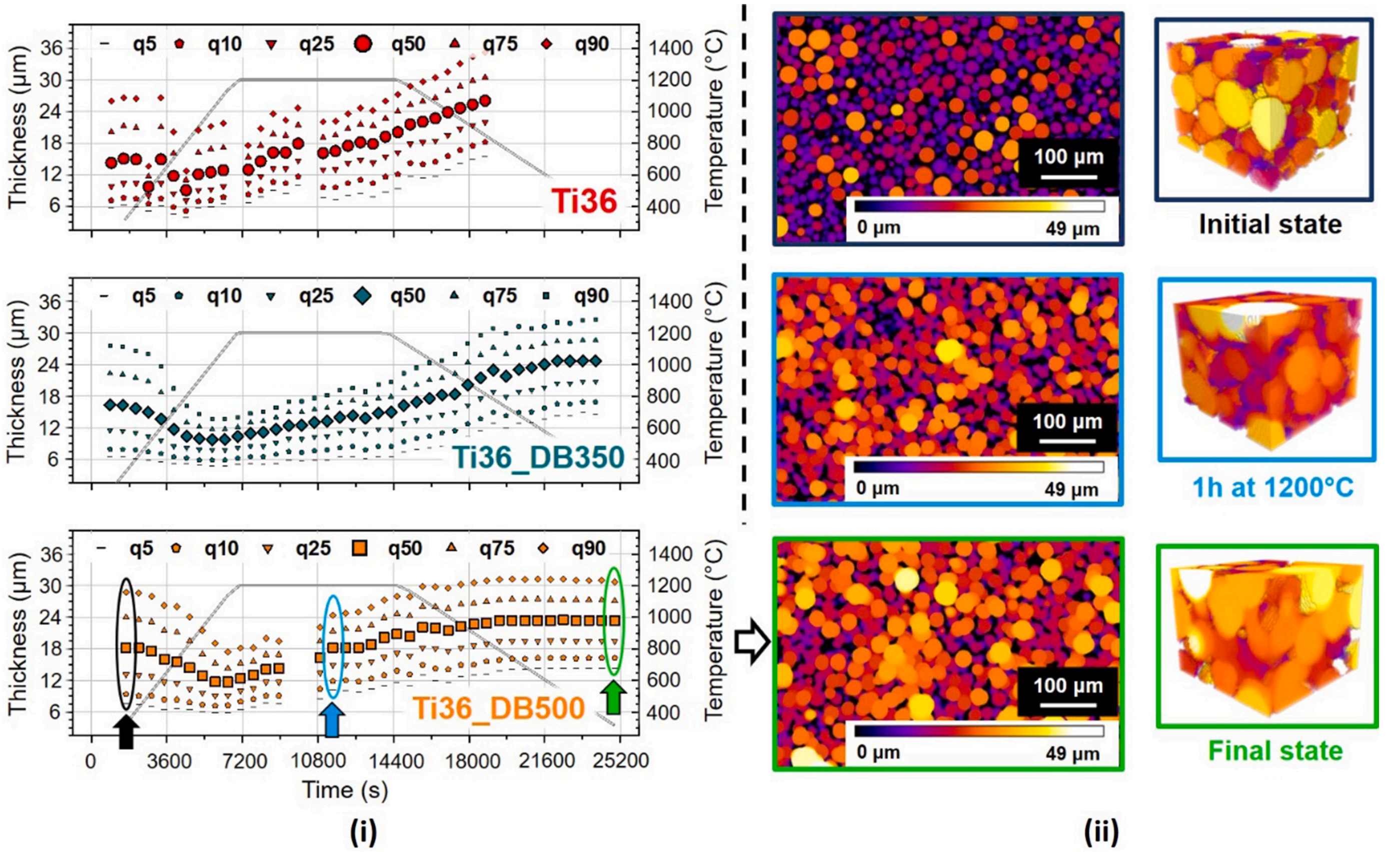

Fig. 3. Solid phase evolution for all samples with (i) the evolution of thickness of the material network and (ii) 2D and 3D (135 × 108 × 133 μm^3) representation of local thickness plugin used on sample TI36_DB500 (one slice and less than 1 vol% of total 3D volume).

Ti36_DB500 at three specific times: the initial state, halfway through the holding step and the final state. Key values q10, q50 and q90 found in the initial granular stack are close to those determined by laser granulometry on the as-atomized powders. From 600 °C to 1200 °C, there is a decrease of the thicknesses associated to the solid phase for all samples, mostly the percentiles above q50. This decrease indicates the onset of the densification during which thin necks between particles form and the volume fraction of material starts increasing. At the early stages of sintering, these interparticular necks just form and thus are small in size, therefore the thicknesses associated with percentiles q90, q75 and q50 decrease significantly. Then, during the holding temperature step, the local thickness of the material network increases continuously, which indicates that growth of the interparticular necks occurs whereas pores are eliminated. As soon as a pore between several particles disappears completely (stage 3 of sintering), a much larger sphere can be used by the Local Thickness plugin to fill these densified particles. Thus, it explains why, at the beginning of the cooling step, the thicknesses associated with the material network are higher than the initial values. During the cooling step, the thicknesses associated to the material network stabilize below 800 °C, *i.e.* sintering stops. At the end, by averaging the three coarse powder samples, the median thickness is around 24.7 ± 1.2 µm with an interquartile range (IQR = q75-q25) around 9.3 ± 1.1 µm. This detailed analysis of the material network can be linked to different densification stages and gives essential information on the sintered part.

3.1.3. *Analysis of the interconnected (open) pore network and the transition toward closed pores*

The evolution of two families of pores were studied separately: the interconnected pores and the closed pores. For all coarse powder samples, the whole porosity is composed of, at least, 85 vol% of the interconnected pores network. Therefore, the evolution of the volume fraction of the interconnected pore is very similar to those of all pores combined whereas the evolution of the volume fraction of closed pores will be commented in more details.

The interconnected pore network initially contains the sum of all the gaps between Ti-6Al-4 V particles, inducing a very complex interconnected pore shape with a sphericity remaining below 0.05 for all samples during the heat treatment. Therefore, it should be described as a network composed of numerous branches (or channels), whose thicknesses were measured using the "Local Thickness" plugin. Fig. 4 shows the evolution of the characteristic thicknesses of the interconnected pores network.

In a similar way to the previous figure, 2D and 3D representations of the distribution of size deduced from the local thickness plugin are shown as well for sample Ti36_DB500 at three specific times: the initial state, halfway through the holding step and the final state. During sintering, the thickness of the interconnected pore is globally stable despite the shrinkage of the interconnected pore network. During all the heat treatment, the average thickness is equal to 7.1 ± 0.4 µm for all samples with an IQR around 3.3 ± 0.4 µm. The insignificant evolution of the thickness, regarding all percentiles, suggests that the decrease in volume of the interconnected pores network only happens by the closure of the branches composing the interconnected pore rather than an isotropic shrinkage. These closures are related to the formation of interparticular necks as commented earlier. At the end, the mean volume fraction represented by the interconnected pore for all samples equals to 12.8 ± 1.5 vol%.

3.1.4. *Analysis of the closed pores*

Fig. 5 shows the evolution of the shape and size of the closed pores exploiting the evolution of four indicators, *i.e.* the volume fraction of all

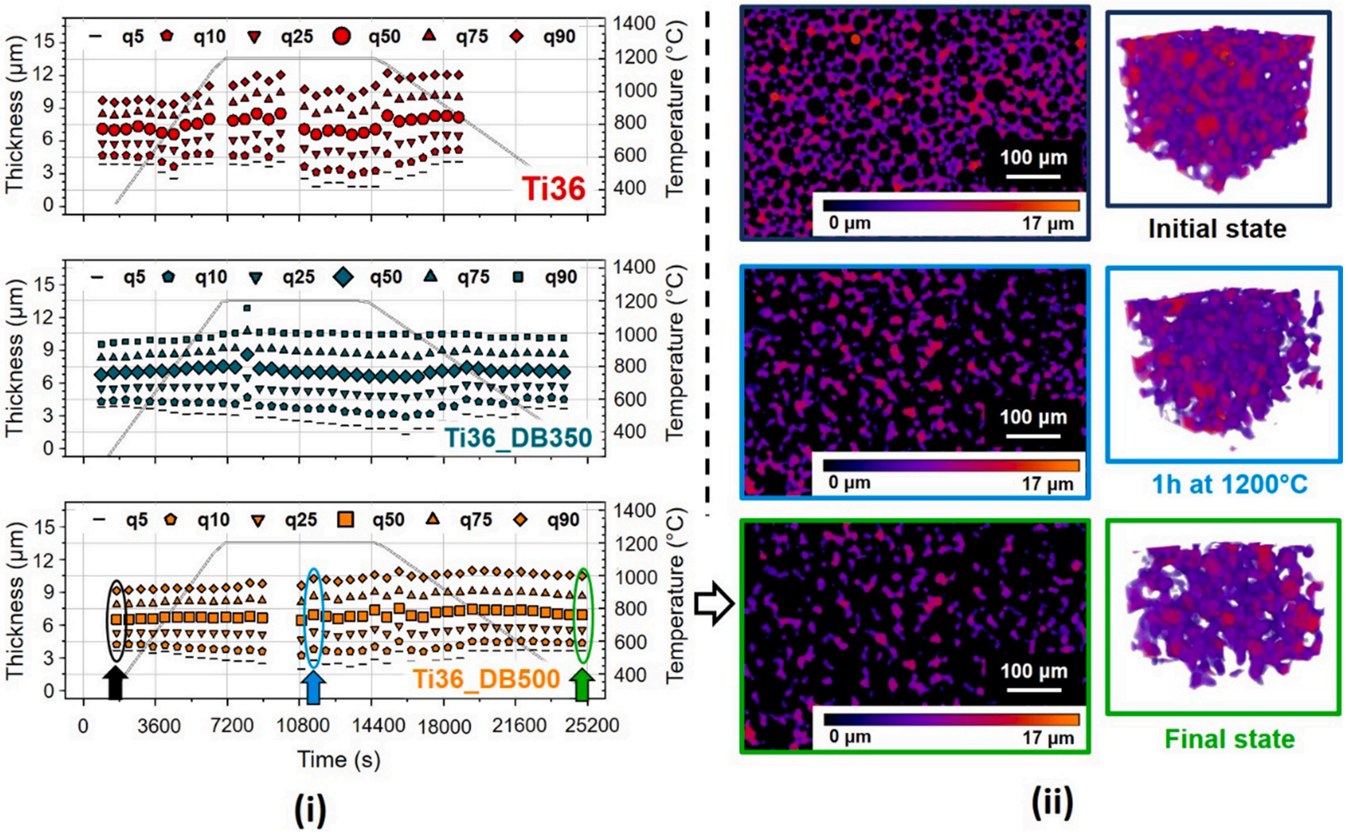

Fig. 4. Interconnected pore evolution for all samples with (i) the evolution of the thickness of their branches and (ii) 2D and 3D (135 × 108 × 133 µm^3) representation of local thickness plugin used on sample Ti36_DB500 (one slice and less than 1 vol% of total 3D volume).

closed pores relative to the whole volume studied, their density (number per mm^3), their average sphericity and their equivalent spherical diameter (ED).

Initially, only few closed spherical pores, with ED of 9.4 ± 0.5 µm (IQR = 7.1 ± 1.4 µm), can be detected. They are internal round (sphericity around 0.9) pores, well known for being present in argon-atomized powders [59]. Then, from around 700 °C to the beginning of the holding temperature step, the number of closed pores increases slightly whereas the size decreases. These first nucleated closed pores have an ED of 4.4 ± 0.4 µm (IQR = 2.5 ± 0.3 µm), hence the volume fraction of closed pores does not increase significantly yet. Then, during all the holding temperature step and in relation with the fragmentation of the interconnected pore, the number and volume fraction of the closed pores increase rather linearly with time, until reaching a maximum at the end of the holding temperature step. Linear fits on this evolution ($R^2 > 0,89$) lead to 3.8 to 5.5 closed pores.mm^{-3}.s^{-1}. In contrast to the fragmentation of the interconnected pores, the formation of closed pores does not slow down during the second part of the holding temperature step. On the contrary, the ED of the closed pores increase so that their volume fraction soars during the second part of the holding temperature step. Besides, the mean sphericity of the closed pores decreases from 0.9 to 0.4. This is in line with the fact that new closed pores are formed from the highly non-spherical interconnected pore. Finally, at the beginning of the cooling step, no more closed pores are formed and typically, below around 800 °C thermal energy is no longer high enough to induce changes in volume fraction, number, size and shape. Few closed pores are even vanishing, which can be explained by a slight evolution of spatial resolution due to thermal contraction. At the end, the ED of the closed pores equals 15.7 ± 2.8 µm (IQR = 10.9 ± 2.5 µm), their volume fraction equals 1.25 ± 0.55 vol% and their number equals 17,300 ± 1600 pores per mm^3. They are highly non-spherical and the ratio between ED (15.7 µm) and thickness (6.3 µm determined by “Local Thickness”) is higher than 2.

To summarize, various microstructural parameters were derived from *in situ* S-µCT, from the evolution of the material network to the evolution of the porosity during free sintering of Ti-6Al-4 V particles. It is demonstrated that different debinding conditions (thus leading to differences in the presence of carbon and oxygen residues) do not significantly impact the densification behavior of the Ti-6Al-4 V powders. Considering the uncertainties related to the experiment, the evolution of the interconnected pores and the closed pores are very similar after different debinding conditions. Globally, the evolution of interconnected pores can be described as a two-step process during which the closed pores are formed continuously by disconnecting from the open porosity. The sintered Ti36 samples are composed of a 12.8 ± 1.5 vol% interconnected pore with 7.1 ± 0.4 µm thick branches and of around 1.25 ± 0.55 vol% of closed pores with an equivalent mean diameter around 15.7 ± 2.8 µm.

Beside the global description, tracking of some individual closed pores was carried out on 665 × 665 × 65 µm^3 vol to analyze their evolution from their nucleation to their eventual closure. Fig. 6 shows the formation of two closed pores from the interconnected network during the beginning of the cooling ramp for sample Ti36_DB500. First, the complex geometry of a part of the interconnected pores network can be observed. From 1060 °C to 900 °C, two branches close without creating closed pores because the parts are still connected to each other. From 900 °C to 740 °C, two other branches close inducing the formation of two closed pores definitively disconnected. As one would expect, the closure of the branches happened in regions where the porosity was thin. Finally, from 740 °C to 315 °C, no significant changes are noticed except the clear spheroidization of the smallest closed pore formed.

3.1.5. Phase transformation kinetics by in situ S-XRD

We used *in situ* S-XRD measurements to quantify the effect of carbon

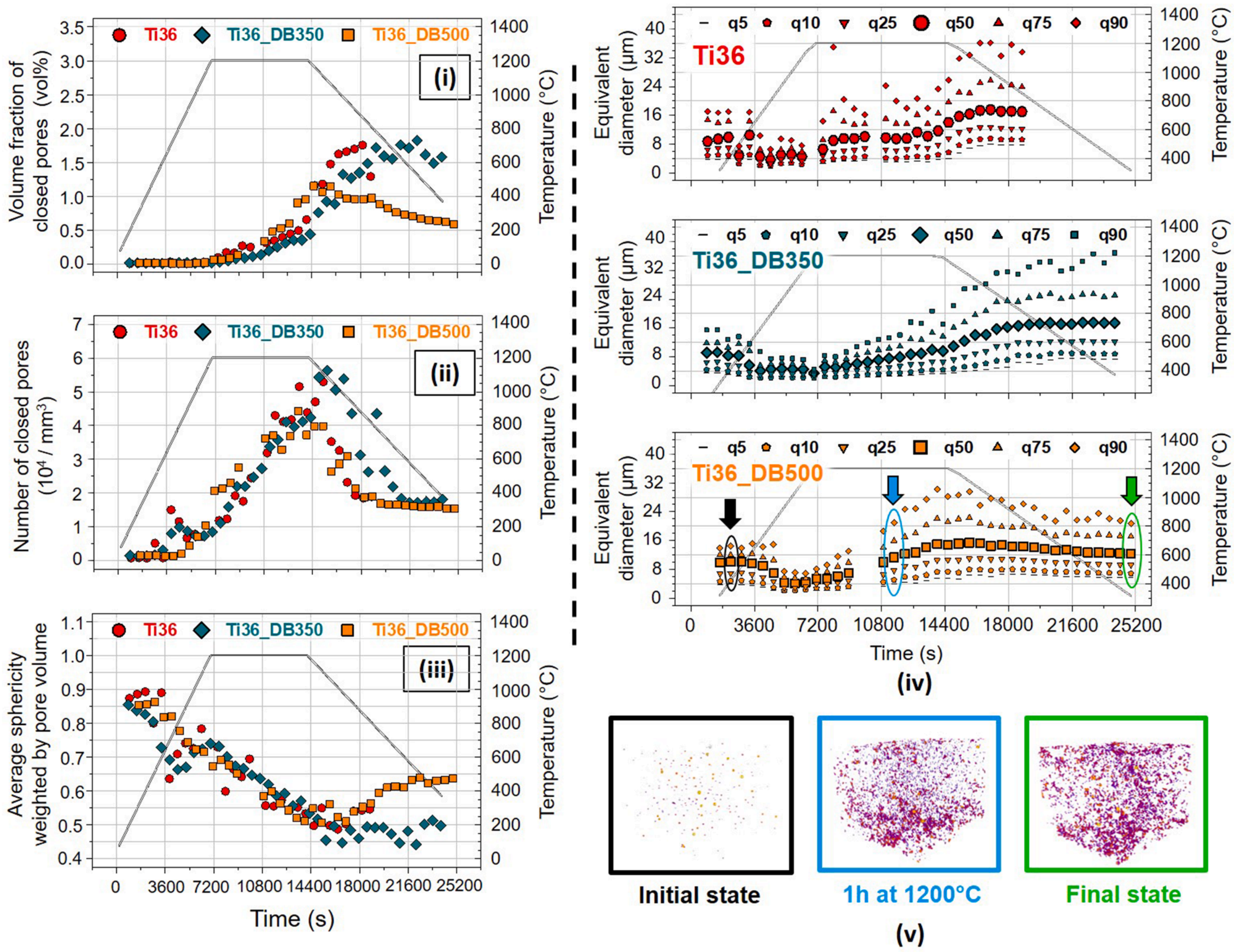

Fig. 5. Evolution of the closed pores regarding (i) their volume fraction, (ii) their number per mm^3, (iii) their mean sphericity (iv) their equivalent diameter for all samples and (v) their 3D representation (whole analyzed volume) for sample Ti36_DB500 using "Local Thickness".

and oxygen residues from debinding on phase transformation and second-phase precipitation during sintering. Contrary to S-µCT, S-XRD acquisition was performed continuously so that the analysis relies on data acquired at a higher temporal frequency.

3.1.6. *Effect of contamination after debinding (coarse powder samples)*

All the diffraction peaks within Ti36 powders were unambiguously attributed to α and β phase. As described in Section 2.2, a fitting procedure was established and enables to represent in Fig. 7 the evolution of the estimated area fraction of the α phase (and, thus, also β phase indirectly) and the evolution of the average lattice parameter in α and β phases.

Upon heating, the formation of β phase begins around 600 °C for all Ti36 samples, which indicates a moderate effect of interstitials contents on the onset of the phase transformation (nucleation and growth of β grains). This is also predicted by thermodynamic calculations (see discussion, Fig. 10). From 600 °C, for Ti36 samples, the evolution of α phase fraction can be fitted using two consecutive sigmoid functions, which indicates the α→β transformation occurs in two stages. The presence of two stages in such a transformation has been reported previously by Bruneseaux et al. during heating of a Ti17 alloy composed initially of a mixture of α and β phase [47]. In that case, the first stage has been associated mainly with the dissolution of the acicular α phase whereas the second stage corresponded to dissolution of the globular α phase. The electron microscopy investigation of the atomized powders (see Fig. 1 of [12]) mainly showed α' martensitic phase but also some rounded α phase in some particles. For as-atomized Ti36 powder (no debinding), the second inflexion point associated with the evolution of the α phase is located at 929 ± 2 °C and no more α phase is detected above 1030 °C whereas α phase is detected up to 1130 °C for Ti36_DB350 and during the holding temperature step at 1200 °C for Ti36_DB500. For these debinded powders, the second inflexion points are located at 978 ± 1 °C and 989 ± 1 °C respectively. Assuming that C and O lie in solid solution, the increased stability of α phase is in line with the increasing C and O contents (see Table 1), as predicted by thermodynamic calculations (see Section 4.4 and Fig. 10). For sample Ti36_DB500, the amount of α stabilizers is high enough to permit presence of α phase at 1200 °C. During the holding temperature step, the slight increase of α phase fraction could be attributed to an oxygen uptake of the sample due to the contact with quartz tube. Finally, upon cooling, α phase is detected again around 1175 °C at the beginning of the cooling step for Ti36_DB350 and around 1100 °C for Ti36, which is once again coherent with the amounts of α stabilizers initially present in the powders. Compared to a previous *ex situ* study [21], titanium carbide was not detected during the cooling step of sample Ti36_DB500. The detection limit is higher in the case of the *in situ* experiments because, among other considerations, a smaller volume of powder is analyzed to carry out S-µCT/S-XRD experiments.

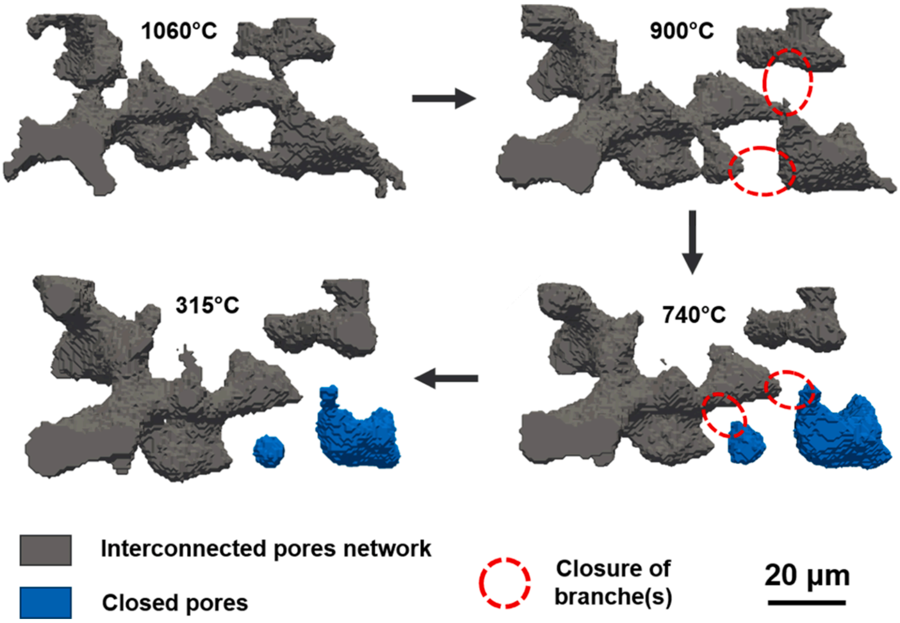

Fig. 6. 3D representation of the formation of closed pores from the interconnected pores network for sample Ti36_DB500.

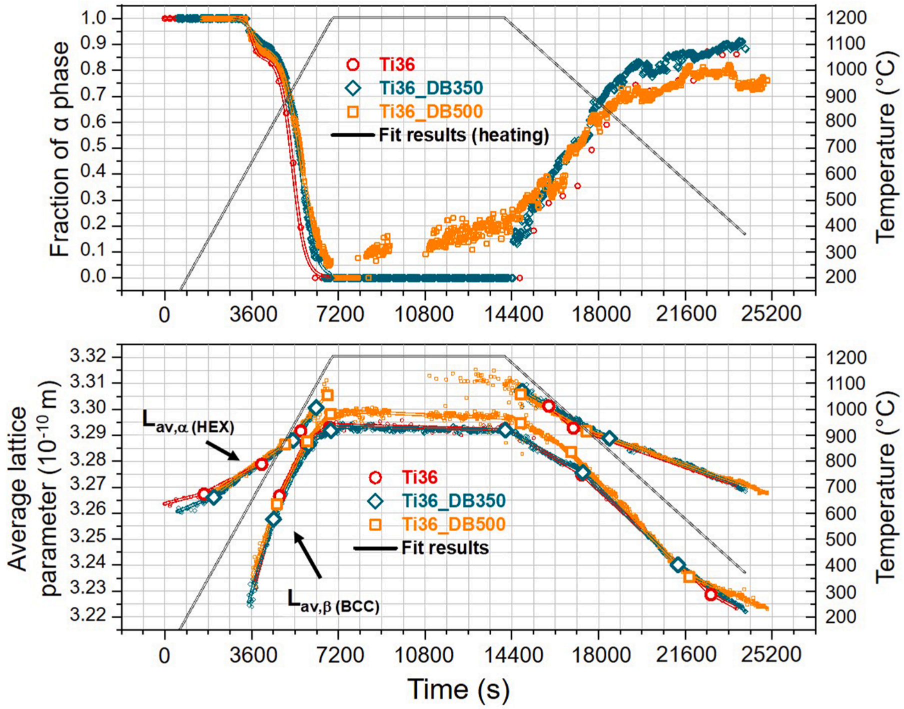

Fig. 7. Description of the α↔β allotropic transformation for Ti36 samples using S-XRD and focusing on the evolution of α-phase fraction (up) and the evolution of the average lattice parameters for both α- and β-phase (down). The evolutions of α-phase fraction during heating and of the average lattice parameters were fitted using two consecutive sigmoid functions and piecewise linear functions, respectively. The larger dots highlight the detected slope changes.

The average lattice parameters of both α ($L_{av,\alpha}$) and β ($L_{av,\beta}$) phases were studied upon sintering, and fitted using piecewise linear functions to detect changes in slopes (see Fig. 7). Their variation, beside linear thermal dilation, can be sensitive to the solid solution and the elastic strain due the mismatch between the lattice of the two phases [47,60]. In the framework of this study, the elastic strain contribution was considered as negligible because the deformation constraint between the phases are likely to dissipate almost instantaneously at high temperatures. Thus, only the change of composition will be discussed even if minor elastic strain contribution might also exist. For the α phase, the interstitials elements C and O are more potent than Al substitutional element, inducing an increase of $L_{av,\alpha}$ with the increase of the concentration of α stabilizers. Concerning the β phase, the increase of the concentration of substitutional stabilizers V induces a decrease of $L_{av,\beta}$.

Heating: Up to 400 °C, the slight evolution of $L_{av,\alpha}$ can mostly be related to a thermal expansion contribution. Then, from 500 °C, β phase, highly rich in V, appears which influences the slope of $L_{av,\alpha}$ so that it deviates from only thermal expansion contribution. Interestingly, the variation of $L_{av,\alpha}$ can be observed even before the unambiguous first detection of β phase. From 500 °C to around 1000 °C, the amount of β phase increases at the expense of the α phase. Similarly to other studies [44,45,47], the increase in the slope of $L_{av,\alpha}$ can be mainly attributed to the increase of the α stabilizers concentration in α phase, since Ti atoms diffuse to form the β phase. Therefore, in the β phase, the concentration of Ti atoms increases relatively to the concentration of V atoms which also explains the high value of the slope. At the end of the heating stage around 1000 °C, the α phase vanishes and the concentration of α stabilizers increases more sharply in the last fraction of α phase. This final sharp increase would explain the increase in the slope from 1000 °C. In parallel, the β phase becomes the majority phase and the increase of the concentration of stabilizers is slighter which results in a slight decrease of the $L_{av,\beta}$ slope.

Holding temperature step: During the holding temperature step at 1200 °C, it can be noticed that the $L_{av,\beta}$ of the sample Ti36_DB500 is significantly higher compared to the two other samples. For this sample, the high concentration of C and O atoms can explain this difference.

Cooling step: Typically, the evolutions of $L_{av,\alpha}$ and $L_{av,\beta}$ during the cooling step can be commented in a reciprocal way compared to the evolutions during the heating step, except that a partial β→α transformation occurs. It should be reminded that cooling rate was equal to 5 K/min whereas the heating rate was equal to 10 K/min. Firstly, the α phase forms with high content of α stabilizers. Then, with increasing amount of α phase, the relative concentration of α stabilizers decreases in the α phase and the slope becomes less sharp. For the β phase, the diffusion of α stabilizers outside the β phase only induces a slight decrease of $L_{av,\beta}$ in the first place. Indeed, as long as the β phase remains in majority, the decrease of the concentration of α stabilizers is limited. This decrease is more important when amount of β phase is lower which explains the greater slope of $L_{av,\beta}$from around 950 °C to around 550 °C. Below 550 °C, the slopes of $L_{av,\alpha}$ and $L_{av,\beta}$ are still high because atoms still diffuse from one phase to another. The *in situ* analysis was not carried out below 400 °C. Below 400 °C, the slopes of $L_{av,\alpha}$ and $L_{av,\beta}$ should be lower and only reflect the linear thermal contribution.

These *in situ* XRD measurements show how a small difference in O and C contents can influence phase stability upon sintering.

3.1.7. Results with a fine powder

Unlike samples with coarse powder, a significant amount of Titanium Carbide ($Ti_{5.73}C_{3.72}$, Ref 01–077–1089) was detected for the sample Ti6_DB350. A *post mortem* analysis of C content in the Ti6_DB350 gave 0.463 ± 0.071 wt%. This initially undesired pollution from inappropriate debinding turned out to be an opportunity to observe *in situ* how titanium carbide together with a high amount of interstitials elements could modify the sintering behavior of Ti-6Al-4 V particles. The Fig. 8 represents the evolution of fraction of the three detected phases computed, as described in part 2.2, alongside with the evolution of the average lattice parameters. The carbides might also exist in the other samples but their amount may be lower than the XRD detection limit. Indeed, the presence of a small amount of $Ti_{5.73}C_{3.72}$ has been reported for sample Ti36_DB500 in a previous study using *ex situ* measurement [21].

According to the *in situ* measurements, carbides start to form almost along with the β phase, *i.e.* around 650 °C during the heating stage. The fraction of titanium carbide is maximum during the holding temperature step and then is no longer detected at the beginning of the cooling step. However, by looking at the final XRD diffractograms, a low intense peak related to the planes (014) of the $Ti_{5.73}C_{3.72}$ phase can still be detected (but not fitted) at the end of the experiment around 300 °C. Given the detection limit of the XRD measurement in the beamline setup, the presence of $Ti_{5.73}C_{3.72}$ must not be negligible in the sintered materials. A clear indication of the diffraction measurement of the fine powder is that the amount of α phase at the end of the heating step did not reach zero and it increased during the holding temperature step. The proportion of the α phase was then clearly higher compared to samples with coarse powder. The second inflexion point relative to the decrease of α phase is

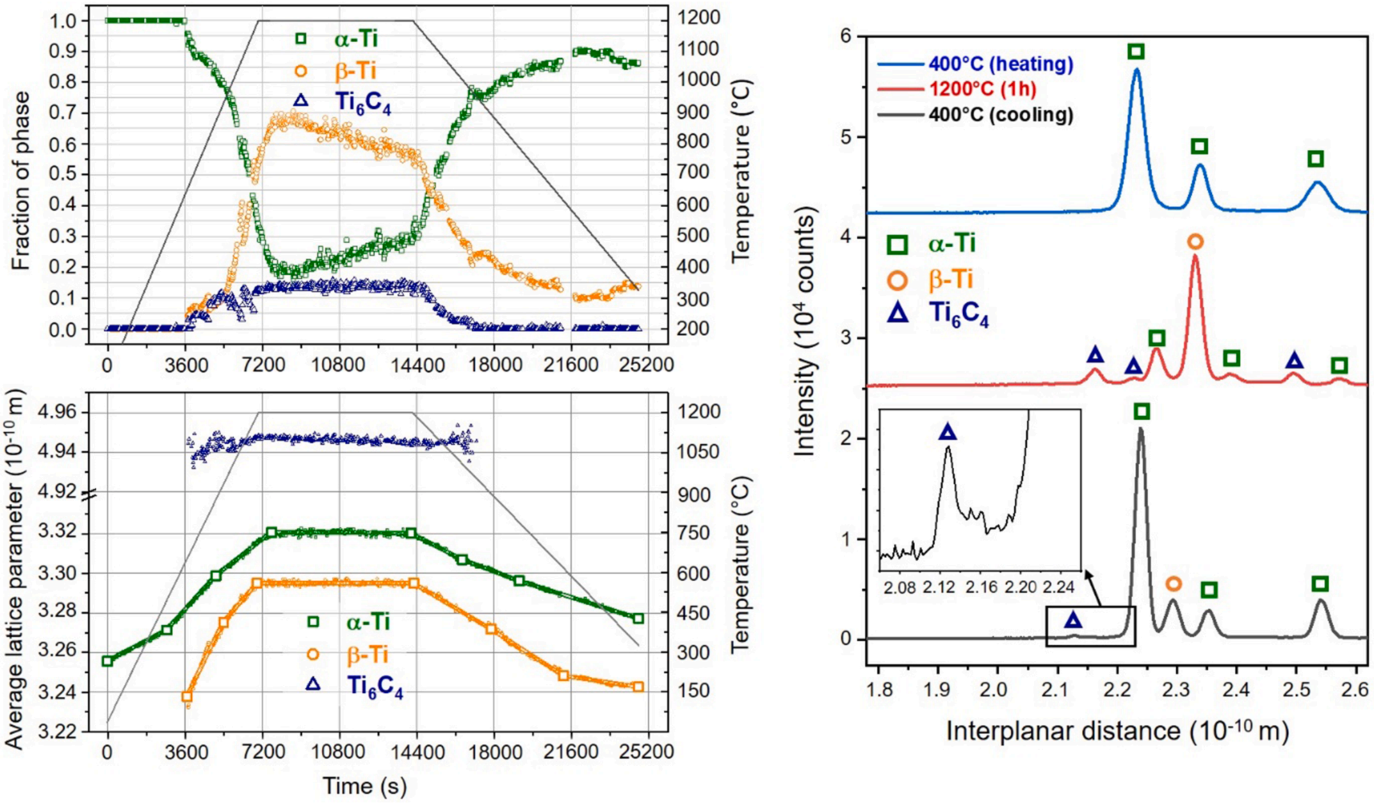

Fig. 8. Analysis of S-XRD of sample Ti6_DB350 with (i) the evolution of phase fraction (up) and evolution of the average length of the lattices (down) for the three detected phases (α-, β- and $Ti_{5.73}C_{3.72}$) and (ii) three diffractograms showing the phases present at the beginning, middle and end of the heat treatment.

at 1186 ± 15 °C which is ~ 200 °C higher than the one of Ti36_DB500 sample. Therefore, the higher initial concentration of C and O stabilizers is in line with both the detection of $Ti_{5.73}C_{3.72}$ phase and the higher stability of the α phase. Concerning the evolution of the average lattice parameters of the different phases, the changes of slope for both α- and β-phase can be explained in the same way as the changes for coarse powder samples, even if the higher concentration of C and O atoms as well as the $Ti_{5.73}C_{3.72}$ formation influences these slopes.

3.1.8. *Local observation of sintering by in situ HT e-SEM*

In addition to the data collected using *in situ* synchrotron XRD/µCT, the formation and growth of interparticles sintering necks was analyzed at high resolution by SEM and *in situ* HT-eSEM (see Fig. 9).

The *in situ* SEM observations in Fig. 9 (a,d) show that the formation of the necks happens at much lower temperature for Ti6 (approximately 750 °C) than for Ti36 (approximately 950 °C), which is expected and in accordance with S-µCT results. Then, for Ti6 and Ti36, the sintering necks grow up to 1050 °C and until the beginning of the holding temperature step, respectively, before their size stabilizes. Necks growth induces the closure of some pores even if, for HT-eSEM analysis, the motion of the particles is hindered by the substrate, which prevents the particle rearrangement during the holding temperature step. There are no clear boundaries between the stages of sintering happening mainly during the heating ramp. For that reason, the analysis of the evolution of the parameters linked to the first stage of sintering (neck size, particles radii, dihedral angles between the spheres, distance between grain centers) is not relevant. Moreover, unlike typical studies dedicated to the first step of sintering [61], the analysis is done on a set of particles in contact and not only on two particles in contact.

The spatial resolution of HT-eSEM enables to detect the growth of crystallites at the surface of Ti-6Al-4 V particles starting at a certain temperature. For the studied samples, the beginning of a significant growth of the crystallites is attributed to the transition from a smooth surface to a surface with outwardly growing needles, which was confirmed by Focused-Ion Beam (FIB) cross-sectionning (see Fig. 9 (b, e)). Interestingly, for Ti36, the detected growth of the crystallites correlates strongly with the formation of the sintering necks. Considering the oriented attachment (OA) mechanisms of polycrystalline particles [62], it is established that a causal link exists between crystallite growth and neck formation: the formation of neck is driven by the reorganization of crystalline planes in the same orientation which promotes the formation of continuous lattice between grains. Then, the growth of the

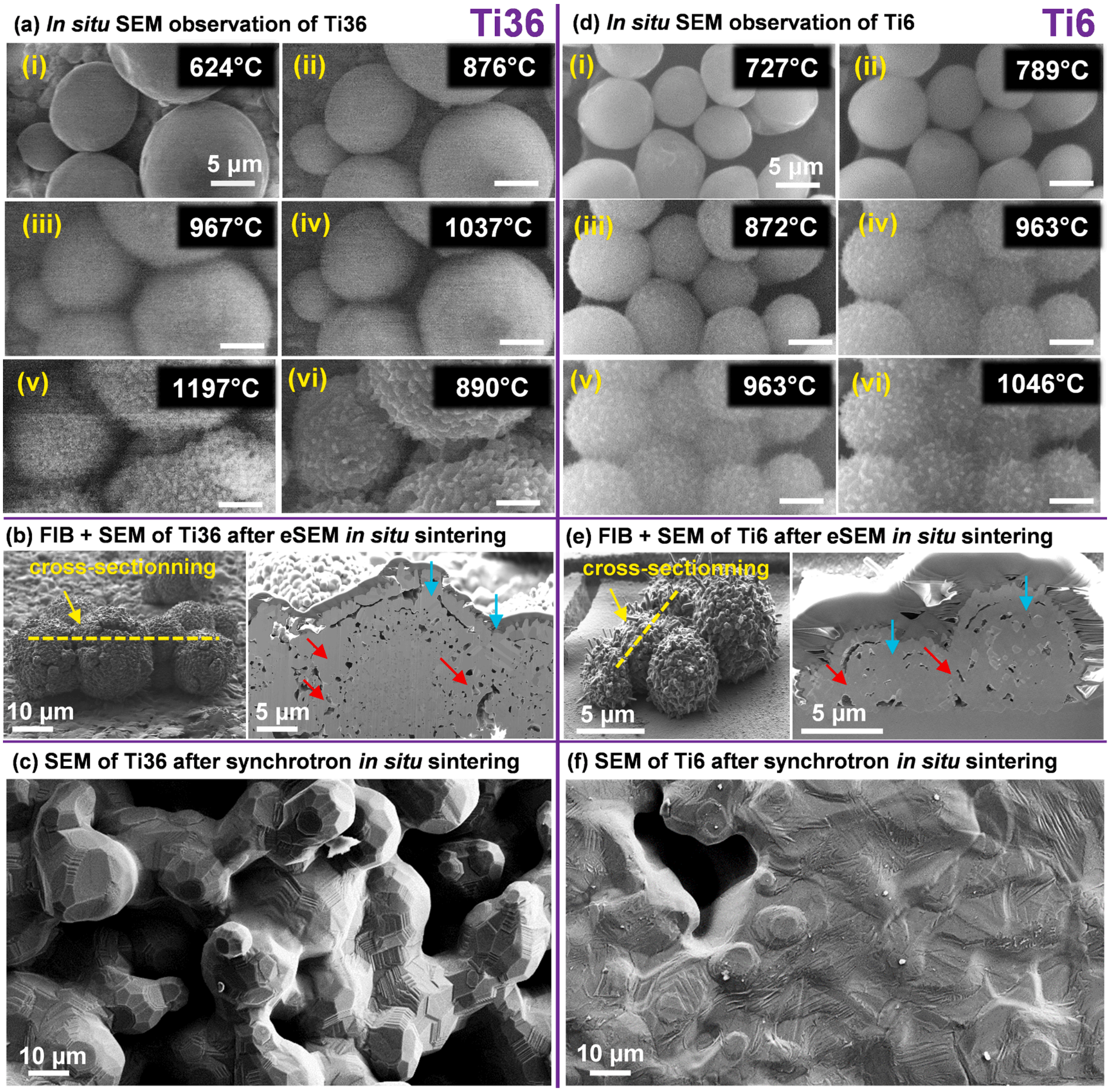

Fig. 9. SEM observations (secondary electrons) of Ti36, resp. Ti6 powders: (a), resp (d) *in situ* eSEM images sequences (i-vi) upon sintering; (b), resp. (e) cross-sections by FIB of powder particles after *in situ* eSEM; red arrows show interparticles necks and blue arrows show grown crystallites around the particles; (c), resp. (f) sintered particles after synchrotron *in situ* sintering.

necks is more attributed to diffusive processes and some crystallites grow at the expense of others that disappear. Finally, for Ti36, the significant growth of the crystallites happens around the α→β transformation which can raise the question about the link between neck formation and the α→β transformation, as discussed later. *Post mortem* SEM observations after synchrotron sintering (see Fig. 9 (c,f)) do not confirm the presence of grown crystallites around particles, which seems to highlight the role of specific conditions (N_2 atmosphere and one monolayer of particles) in the eSEM.

The HT-eSEM allowed to analyze the system at deeper local scale and highlighted fine phenomena which could not be properly studied using S-μCT, in particular for the fine Ti6 powders. This complementary *in situ* characterization confirmed the much more rapid densification kinetics for the fine powder, mainly achieved during the heating ramp.

4. Discussion

4.1. Global densification kinetics

Firstly, the evolution of the porosity (see Fig. 2) can be further commented. Especially, in the case of coarse powder samples, the evolution of the porosity does not present regular sigmoid shape during the holding temperature step. In order to highlight this observation, sigmoid-shaped porosity evolutions (see Fig. 2) were fitted using an equation combining two Avrami-like equations (see (Eq. (4)) for Ti36 coarse powder whereas only one Avrami-like equation was sufficient to describe properly the evolution of the porosity for the fine powder Ti6 sample. All the fits converged and the fitting parameters are reported in Table 3. Even if Avrami-like equations are normally used to describe the kinetics of the diffusional phase transformations [63], they were used in this study to highlight the presence of two inflection points and, therefore, of two different kinetics associated with the reduction of the porosity.

Despite some variations between coarse powder samples, the constant n_1 associated with the first sigmoid is around 6 whereas the constant n_2 is around 4. Even if the use of an Avrami-like equation is debatable, these two distinct values could mean that there is a second sintering mechanism which overrides the first during the sintering. The transition between the first and second kinetics of the shrinkage of the porosity happens between 20 and 25 vol% for coarse powder Ti36 samples. Previous studies used dilatometric analyses to compute activation energies related with the sintering of Ti-6Al-4 V alloys [28, 32]. Cabezas et al. stated that volume diffusion mechanism is predominant when the porosity is above 20 vol% or below 10 vol%. Between 10 and 20 vol%, the sintering would rather be controlled by grain-boundary diffusion mechanism. Consequently, the results presented in our study seem to be in accordance with the hypothesis of Cabezas et al. [28]. The complete suppression of closed pores would require longer holding times at high temperature. For the fine powder Ti6 sample, the value of the Avrami constant is once again around 6. In this case, sintering occurs too quickly for the grain-boundary diffusion mechanism to be detected. To sum up, there would be successive mechanisms leading to the densification of the Ti-6Al-4 V powder but several temperatures should be tested to derive activation energies and conclude on the sintering mechanisms.

$$Porosity = P_{final} + \left(P_{initial} - P_{final}\right)\left(f \times e^{-k_1 t^{n_1}} + (1-f) \times e^{-k_2 t^{n_2}}\right) \qquad \text{(Eq. 4)}$$

4.2. Sintering mechanisms: from interconnected open porosity to closed pores

The densification is the consequence of sintering mechanisms occurring at the microscopic scale, which induces an evolution of the material network, of the interconnected pores and of the closed pores. Considering the uncertainties related to the experiment, these evolutions are very similar for the coarse powder Ti36 samples. Table 4 sums up the different results of the analysis of the three different microstructural features with emphasis on the evolution of their size for the Ti36 samples. Therefore, relative to the heat treatment, the densification can be divided into five steps:

(i) from room temperature to 700 °C: no significant change;
(ii) from 700 °C to 1200 °C: interparticular necks start to form, which close few branches of the interconnected pores network. The *in situ* HT-eSEM analysis confirmed the onset of necks formation above 700 °C. The decrease in volume of the interconnected pores network starts but remains limited (see Fig. 2). It should be noted that the Ti-6Al-4 V powder is polydisperse so that the temperature associated with the necks formation between two particles depends on these particles respective size. It is thought that the first small closed pores were formed mostly where they were already isolated in the interconnected pores network like, for example, at the end of a branch.

Table 3
Parameters of the fitted curves representing the evolution of the porosity.

Samples		Ti36	Ti36_DB350	Ti36_DB500	Ti6_DB350
$P_{initial}$ – initial porosity (vol%)		41.3 ± 0.2	41.1 ± 0.4	35.9 ± 0.2	44.0 ± 0.7
P_{final} – final porosity (vol%)		12.2 ± 0.6	13.5 ± 0.5	14.7 ± 0.1	0.5 ± 0.3
f – fraction of first Avrami equation		0.48 ± 0.12	0.34 ± 0.22	0.54 ± 0.26	1
First Avrami function					
k_1 – Avrami constant (10^{-15})		3.7 ± 9.5	1.4 ± 8.8	21.9 ± 113.9	22.7 ± 33.9
n_1 – Avrami constant		6.3 ± 0.3	6.3 ± 0.7	6.0 ± 0.6	6.2 ± 0.1
First inflection point (IP_1)	Temperature (°C)	1200	1200	1200	1083 ± 6
	Times (mn) relative to the holding step	12.6 ± 1.3	30.4 ± 3.9	14.9 ± 2.5	- 12.4 ± 0.6
Second Avrami function					
k_2 – Avrami constant (10^{-7})		5.3 ± 56.5	0.9 ± 14.5	0.9 ± 1.6	
n_2 – Avrami constant		3.9 ± 1.1	4.1 ± 1.6	4.4 ±1.9	
Second inflection point (IP_2)	Temperature (°C)	1200	1200	1200	
	Times (mn) relative to the holding step	91.8 ± 1.6	118.1 ± 3.2	70.7 ± 4.3	

Table 4

Different steps linked to the evolution of the material network, of the interconnected pores and of the closed pores, for coarse powder Ti36 samples (average values).

	(i) Initial state + Heating up to ≈ 700 °C	(ii) Heating from ≈ 700 °C to 1200 °C	(iii) Holding temperature step (1200 °C)	(iv) Cooling from 1200 °C to ≈ 850 °C	(v) Cooling up to final state
Material network (Local Thickness)	**Granular stack** $q_{50} = 16.3 \pm 1.6$ µm (IQR = 10.6 ± 0.1 µm)	**Formation of interparticular necks** $q_{50} \searrow 11.3 \pm 1.4$ µm (IQR = 5.6 ± 1.7 µm)	**Growth of interparticular necks** $q_{50} \nearrow$	**Growth of interparticular necks** $q_{50} \nearrow$	**Stabilization** $q_{50} = 24.7 \pm 1.2$ µm (IQR= 9.3 ± 1.1 µm)
Inter-connected pores (Local Thickness)	**Voids between particles** $q_{50} = 6.8 \pm 0.3$ µm (IQR = 2.7 ± 0.1 µm)	**Beginning of shrinkage** $q_{50} \rightarrow$	**Closure at the end of branches** (most shrinkage) $q_{50} \rightarrow$	**Closure at the end of branches** (slowing) $q_{50} \rightarrow$	**Stabilization** $q_{50} = 7.4 \pm 0.7$ µm (IQR = 3.2 ± 0.3 µm)
Closed pores (Equivalent diameter)	**Pores inside particles** $q_{50} = 9.4 \pm 0.5$ µm (IQR = 7.1 ± 1.4 µm)	**Formation of small closed pores** $q_{50} \searrow 4.4 \pm 0.4$ µm (IQR = 2.5 ± 0.3 µm)	**Formation of more and larger pores** $q_{50} \nearrow$	**Slight decrease of number of pores** $q_{50} \nearrow$	**Stabilization** $q_{50} = 15.7 \pm 2.8$ µm (IQR = 10.9 ± 2.5 µm)

(iii) during the holding step temperature, the shrinkage accelerates and the interparticular necks grow. The branches of the interconnected pores network close more and more, inducing the formation of numerous closed pores. These pores can be highly non-spherical - as they can be formed at crossroad of branches - and can be rather large.

(iv) from 1200 °C to 850 °C, these phenomena continue during the beginning of the cooling step.

(v) Below 850 °C, there are no significant changes of the material network, of the interconnected pores or of the closed pores. By averaging the three samples, the sintered materials are composed of 12.8 ± 1.5 vol% of interconnected pore with 7.1 ± 0.4 µm thick branches, of around 1.25 ± 0.55 vol% of closed pores with an equivalent mean diameter around 15.7 ± 2.8 µm and the rest of a 24.7 ± 1.2 µm thick material network.

4.3. *Link between α→β phase transformation and densification kinetics*

As suggested in previous works on Ti alloys sintering [28], a causal link may exist between the densification and the α→β phase transformation due to a large increase of self-diffusion coefficient of Ti related to the α→β transformation [64]. In that framework, *in situ* S-XRD/µCT coupling represents an interesting opportunity to discuss this hypothesis.

For coarse powder samples, the densification starts around 1000 °C, which is in accordance with the second inflexion points associated to the α→β transformation. Indeed, around 950 °C, the β phase becomes the majority phase (see Fig. 7). However, some other observations can be put forward to question the existence of such a causal link between the phase transformation and the densification. Firstly, the α→β transformation begins in reality at lower temperature, *i.e.* around 600 °C, without inducing the start of the shrinkage. Moreover, for sample Ti36_DB500, the significant amount of α phase remaining during the holding step temperature does not lead to significant changes in the densification compared to sample Ti36. Finally, it can also be underlined that, for the fine powder sample Ti6_DB350, the densification starts even at lower temperature around 900 °C although the stability of the α phase is increased due to large amount of α stabilizers. In that case, the effect of the powder particle size is clearly predominant compared to the phase transformation. Thus, the onset of densification can neither be clearly associated with the beginning of the α→β transformation nor with the moment when the β phase is the majority phase. Consequently, the *in situ* S-XRD/ µCT results permit to refute the existence of a strong causal link between the densification and the α→β transformation.

4.4. *Effect of interstitials (inherited from debinding) on phase transformation, carbides precipitation and densification kinetics*

For Ti36 coarse powder, the carbon and oxygen uptakes do not significantly influence the densification kinetics. But they increase the stability of α phase toward the higher temperatures, which was confirmed by thermodynamic calculations (see Fig. 10(i)). Whether carbides were formed or not is questionable but at least no peak associated with carbide was detected in these samples whereas the formation of the $Ti_{5.73}C_{3.72}$ phase was detected upon sintering of Ti6_DB350 sample. Two conditions shall be met for this precipitation: (i) the carbon content must exceed the solubility of C in Ti-6Al-4 V and (ii) the time or temperature must be long or high enough to allow diffusion. Using the fitted solubility products $K_{Ti_6C_4}$ from TTTI3 [65] thermodynamic database, the C solubility limit was computed in both α- and β-phases for temperatures and concentrations of O atoms ranging from 300 to 1200 °C and from 0 to 1 wt% respectively (see Fig. 10).

For the Ti36 samples, the solubility limit of C in the β-Ti phase at 1200 °C was too high (0.344 wt% for 0.335 wt% O) compared to the C content (<0.2 wt%), which makes unlikely the precipitation of Ti_6C_4 at 1200 °C. For this amount of C, precipitation of carbides in the β phase can only occur during cooling for a temperature domain ranging from 1000 to 700 °C where the solubility limit is exceeded (0.175 wt% at 975 °C for 0.335 wt% O) and where the mobility and driving forces are high enough for precipitation of Ti_6C_4 to occur in the β phase, as detailed in a previous work [21]. Nevertheless, the β→α transformation has been fixed at around 600 °C for the modeling [21] so that partial diffusion of C and dissolution of Ti_6C_4 in the forming α phase have not been considered during cooling from 1000 to 600 °C. Unfortunately, the detection limit of S-XRD did not enable to improve the model in this regard through the *in situ* detection of Ti_6C_4. Dealing with the 0.463 wt% of C atoms in the fine powder, the solubility limit of C in the Ti-β phase was exceeded at 1200 °C (even considering only 0.102 wt% of O atoms, this solubility limit of C should be 0.369 wt%). Therefore, precipitation of titanium carbide can occur at 1200 °C. Interestingly, the formation of Ti_6C_4 happens from 650 °C in conjunction with the α→β transformation. From 650 °C, the mobility and driving forces must be high enough to induce precipitation of Ti_6C_4 even in the α phase where the solubility limit of C equals to 0.322 wt% (0.102 wt% O). With increasing amount of β phase with lower solubility limit of C, Ti_6C_4 forms more largely in the system. Despite the increasing solubility limit of C in the α phase with temperature, all C atoms cannot be contained in the remaining α phase. During cooling, almost total dissolution of the titanium carbide happens in conjunction with the β→α transformation. With increasing amount of the α phase, the amount of C atoms that can be “stored” in the α phase increases significantly. However, the solubility limit of C in the α phase decreases with temperature. Therefore, all C atoms cannot be contained in the α and β phases at the end, that is why Ti_6C_4 is detected in the last scan despite the detection limit (see Fig. 8).

5. Conclusion

Sintering of Ti-6Al-4 V powders was investigated using *in situ* synchrotron coupled XRD/µCT measurements and HT-SEM observations. The powders were studied as-atomised or previously 3D printed by

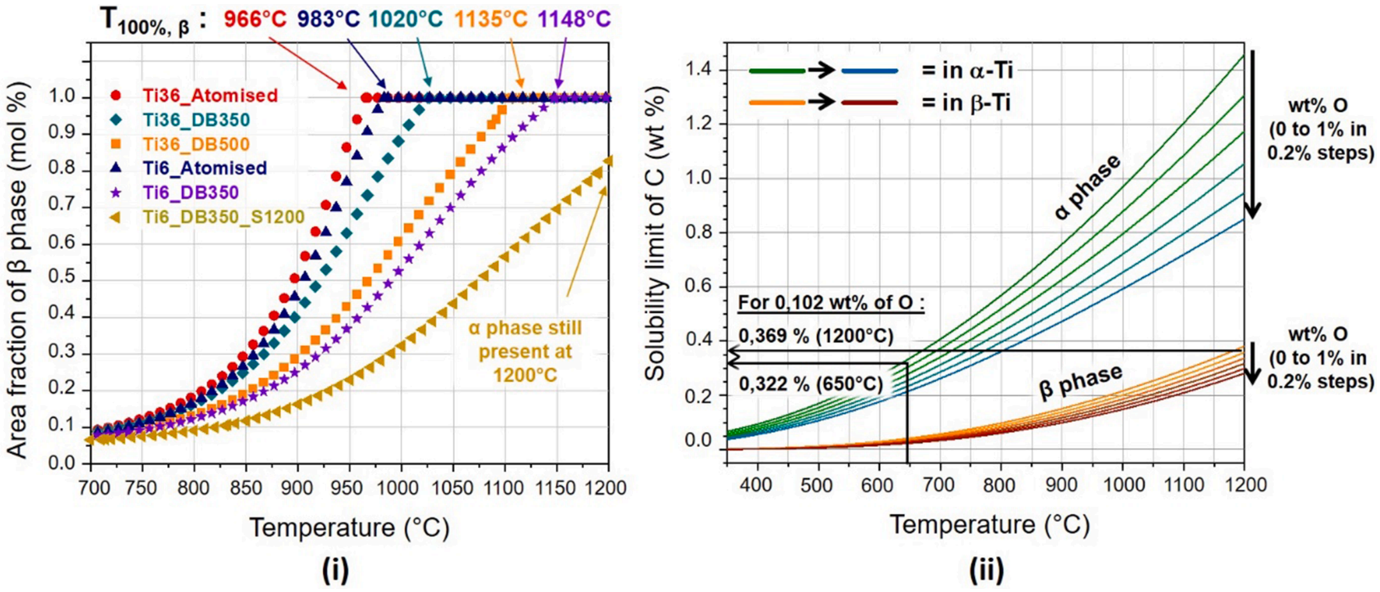

Fig. 10. Thermodynamic calculations (ThermoCalc, TTTi3) in function of temperature of (i) the β phase formation depending on the C and O contents in studied powders and (ii) of solubility limit of C (wt%) depending on the O content (wt%) relative to the precipitations of Ti_6C_4.

direct-ink writing and debinded under different conditions, so that the influence of carbon and oxygen contaminations on the sintering behavior could be studied. Particularly adapted to the study of titanium alloys, this coupling allowed for the first time to jointly follow *in situ* the evolution of the porosity as well as α↔β phase transformation during non-isothermal sintering treatment.

Firstly, based on the study of samples debinded under different conditions, it was shown that the densification was not significantly impacted by the presence of organic residues. Despite higher amount of residuals, the fine powder Ti6 sample densifies completely at lower temperature. For the coarse powder Ti36 samples, the S-μCT enabled to describe the densification kinetics and the sintering mechanisms, from the split of the open porosity to the evolution of new closed pores. The final porosity was composed of a 12.8 ± 1.5 vol% interconnected pore with 7.1 ± 0.4 μm thick branches and of around 1.25 ± 0.55 vol% of closed pores with an equivalent mean diameter between 15.7 ± 2.8 μm. The identification of two kinetics associated with the shrinkage was discussed considering the possible sintering mechanisms but isothermal treatments shall be done to derive accurately the activation energy of diffusion-driven processes involved here.

Secondly, the analysis of S-XRD data showed the strong dependency of the α phase stability on the amount of additional C and O atoms due to the debinding treatment. The α↔β phase transformation occurring during the sintering treatment was precisely described regarding the area and position of the detected peaks. Detection of Ti_6C_4 for fine powder sample was clearly attributed to the higher amount of C atoms detected in the material.

Then, *in situ* S-XRD/μCT coupling allowed to refute the existence of a strong causal link between the sintering of Ti-6Al-4 V materials and the α→β transformation. It was demonstrated that the temperature and the powder size are more predominant factors for sintering of Ti-6Al-4 V.

This multi-scale *in situ* study of solid sintering can be used to identify the effect of powder particle size on the contamination / densification trade-off when the fabrication of functionally graded materials, such as porosity-graded scaffolds or implants, is targeted.

The authors think that this work, based on coupled S-XRD and S-μCT, can be the basis of numerous other works focusing on the sintering of metallic or ceramic powder as well as hybrid systems such as ceramic or metal matrix composites (Eqn (2), Eqn (3)).

Declaration of Competing Interest

The authors declare that they have no known competing financial interests or personal relationships that could have appeared to influence the work reported in this paper.

Acknowledgements

The authors acknowledge SOLEIL and the beamline Psiché for provision of synchrotron radiation facilities. This work was partly supported by LABEX MANUTECH-SISE (ANR-10-LABX-0075) of the Universite de Lyon, within the program "Investissements d'Avenir" (ANR-11-IDEX-0007) operated by the French National Research Agency (ANR). The authors acknowledge the Consortium Lyon Saint-Etienne de Microscopie (CLYM, FED 4092) for the access to the microscopes.

Supplementary materials

Supplementary material associated with this article can be found, in the online version, at doi:10.1016/j.actamat.2023.118723.

References

[1] S.T. Tshephe, O.S. Akinwamide, E. Olevsky, A.P. Olubambi, Additive manufacturing of titanium-based alloys- A review of methods, properties, challenges, and prospects, Heliyon 8 (2022) e09041, https://doi.org/10.1016/j.heliyon.2022.e09041.

[2] E. Alabort, Y.T. Tang, D. Barba, R.C. Reed, Alloys-by-design : A low-modulus titanium alloy for additively manufactured biomedical implants, Acta Mater. 229 (2022), 117749, https://doi.org/10.1016/j.actamat.2022.117749.

[3] X. Pei, L. Wu, H. Lei, C. Zhou, H. Fan, Fabrication of customized Ti6AI4V heterogeneous scaffolds with selective laser melting : Optimization of the architecture for orthopedic implant applications, Acta Biomater. 126 (2021) 485–495, https://doi.org/10.1016/j.actbio.2021.03.040.

[4] J.L. Bartlett, X. Li, An overview of residual stresses in metal powder bed fusion, Addit. Manuf. 27 (2019) 131–149, https://doi.org/10.1016/j.addma.2019.02.020.

[5] T.A. Baer, J. Cesarano III, P. Calvert, J. Cesarano, T.A. Baer, P. Calvert, Recent developments in freeform fabrication of dense ceramics from slurry deposition, in: Solid Freeform Fabrication Proceedings, September 1997, 1997, pp. 25–32, https://doi.org/10.2172/554831.

[6] J.E. Smay, J. Cesarano, J.A. Lewis, Colloidal inks for directed assembly of 3-D periodic structures, Langmuir 18 (2002) 5429–5437, https://doi.org/10.1021/la0257135.

[7] J.A. Lewis, Direct ink writing of 3D functional materials, Adv. Funct. Mater. 16 (2006) 2193–2204, https://doi.org/10.1002/adfm.200600434.

[8] P. Singh, V.K. Balla, S.V. Atre, R.M. German, K.H. Kate, Factors affecting properties of Ti-6Al-4 V alloy additive manufactured by metal fused filament fabrication, Powder Technol. 386 (2021) 9–19, https://doi.org/10.1016/j.powtec.2021.03.026.

[9] A. Mostafaei, A.M. Elliott, J.E. Barnes, F. Li, W. Tan, C.L. Cramer, P. Nandwana, M. Chmielus, Binder jet 3D printing — Process parameters, materials, properties, modeling, and challenges, Prog. Mater. Sci. 119 (2021), 100707, https://doi.org/10.1016/j.pmatsci.2020.100707.

[10] E. Stevens, S. Schloder, E. Bono, D. Schmidt, M. Chmielus, Density variation in binder jetting 3D-printed and sintered Ti-6Al-4 V, Addit. Manuf. 22 (2018) 746–752, https://doi.org/10.1016/j.addma.2018.06.017.

[11] Q. Chen, G.A. Thouas, Metallic implant biomaterials, Mater. Sci. Eng. R Rep. 87 (2015) 1–57, https://doi.org/10.1016/j.mser.2014.10.001.

[12] M. Coffigniez, L. Gremillard, S. Balvay, J. Lachambre, J. Adrien, X. Boulnat, Direct-ink writing of strong and biocompatible titanium scaffolds with bimodal interconnected porosity, Addit. Manuf. 39 (2021) 2214–8604, https://doi.org/10.1016/j.addma.2021.101859.

[13] R. Shah, B. Gashi, S. Hoque, M. Marian, A. Rosenkranz, Enhancing mechanical and biomedical properties of protheses - Surface and material design, Surf. Interf. 27 (2021), https://doi.org/10.1016/j.surfin.2021.101498.

[14] V. Karageorgiou, D. Kaplan, Porosity of 3D biomaterial scaffolds and osteogenesis, Biomaterials 26 (2005) 5474–5491, https://doi.org/10.1016/j.biomaterials.2005.02.002.

[15] S.K. Lan Levengood, S.J. Polak, M.B. Wheeler, A.J. Maki, S.G. Clark, R.D. Jamison, A.J. Wagoner Johnson, Multiscale osteointegration as a new paradigm for the design of calcium phosphate scaffolds for bone regeneration, Biomaterials 31 (2010) 3552–3563, https://doi.org/10.1016/j.biomaterials.2010.01.052.

[16] S.J. Polak, L.E. Rustom, G.M. Genin, M. Talcott, A.J. Wagoner Johnson, A mechanism for effective cell-seeding in rigid, microporous substrates, Acta Biomater. 9 (2013) 7977–7986, https://doi.org/10.1016/j.actbio.2013.04.040.

[17] F.H. Beck, Effect of Hydrogen on the Mechanical Properties of Titanium and Its Alloys, Ohio State University Report. Dissertati, 1975, pp. 1–15.

[18] R.M. German, Supersolidus Liquid-Phase Sintering of Prealloyed Powders, 28, 1997, pp. 1553–1567, https://doi.org/10.1007/s11661-997-0217-0.

[19] T. Ebel, Metal Injection Molding (MIM) of Titanium and Titanium Alloys, 2nd ed., Elsevier Ltd., 2019 https://doi.org/10.1016/B978-0-08-102152-1.00023-4.

[20] A. Dehghan-manshadi, M.J. Bermingham, M.S. Dargusch, D.H. Stjohn, M. Qian, Metal injection moulding of titanium and titanium alloys : Challenges and recent development, Powder Technol. 319 (2017) 289–301, https://doi.org/10.1016/j.powtec.2017.06.053.

[21] M. Coffigniez, L. Gremillard, M. Perez, S. Simon, C. Rigollet, E. Bonjour, P. Jame, X. Boulnat, Modeling of interstitials diffusion during debinding/sintering of 3D printed metallic filaments: Application to titanium alloy and its embrittlement, Acta Mater. 219 (2021), https://doi.org/10.1016/j.actamat.2021.117224.

[22] J.P. Li, J.R. De Wijn, C.A. Van Blitterswijk, K.D.E Groot, Porous Ti6Al4V scaffolds directly fabricated by 3D fibre deposition technique: Effect of nozzle diameter, J. Mater. Sci. 16 (2005) 1159–1163, https://doi.org/10.1007/s10856-005-4723-6.

[23] J.P. Li, J.R. De Wijn, C.A. Van Blitterswijk, K. De Groot, Porous Ti6Al4V scaffold directly fabricating by rapid prototyping: Preparation and in vitro experiment, Biomaterials 27 (2006) 1223–1235, https://doi.org/10.1016/j.biomaterials.2005.08.033.

[24] H. Elsayed, P. Rebesan, G. Giacomello, M. Pasetto, C. Gardin, L. Ferroni, B. Zavan, L. Biasetto, Direct ink writing of porous titanium (Ti6Al4V)lattice structures, Mater. Sci. Eng. C 103 (2019), https://doi.org/10.1016/j.msec.2019.109794.

[25] H. Elsayed, N. Novak, M. Vesenjak, F. Zanini, S. Carmignato, L. Biasetto, The effect of strut size on microstructure and compressive strength of porous Ti6Al4V lattices printed via Direct Ink Writing, Mater. Sci. Eng. A 787 (2020), https://doi.org/10.1016/j.msea.2020.139484.

[26] M. Qian, Y.F. Yang, S.D. Luo, H.P. Tang, Pressureless Sintering of Titanium and Titanium alloys: Sintering densification and Solute Homogenization, Elsevier Inc., 2015, https://doi.org/10.1016/B978-0-12-800054-0.00012-5.

[27] M. Qian, G.B. Schaffer, C.J. Bettles, Sintering of titanium and its alloys, Sinter. Adv. Mater. (2010) 324–355, https://doi.org/10.1533/9781845699949.3.324.

[28] J.L. Cabezas-Villa, J. Lemus-Ruiz, D. Bouvard, O. Jiménez, H.J. Vergara-Hernández, L. Olmos, Sintering study of Ti6Al4V powders with different particle sizes and their mechanical properties, Int. J. Miner. Metal. Mater. 25 (2018) 1389–1401, https://doi.org/10.1007/s12613-018-1693-5.

[29] Z.Q. Yan, F. Chen, Y.X. Cai, J. Yin, Influence of particle size on property of Ti-6Al-4 V alloy prepared by high-velocity compaction, Trans. Nonferrous Metal Soc. Chin. 23 (2013) 361–365, https://doi.org/10.1016/S1003-6326(13)62470-X.

[30] I.H. Oh, N. Nomura, N. Masahashi, S. Hanada, Mechanical properties of porous titanium compacts prepared by powder sintering, SCR Mater. 49 (2003) 1197–1202, https://doi.org/10.1016/j.scriptamat.2003.08.018.

[31] J. Chávez, L. Olmos, O. Jiménez, D. Bouvard, E. Rodríguez, M. Flores, Sintering behaviour and mechanical characterisation of Ti64/xTiN composites and bilayer components, Powder Metallurgy 60 (2017) 257–266, https://doi.org/10.1080/00325899.2017.1280585.

[32] X. Xu, P. Nash, Sintering mechanisms of Armstrong prealloyed Ti-6Al-4 V powders, Mater. Sci. Eng. A 607 (2014) 409–416, https://doi.org/10.1016/j.msea.2014.03.045.

[33] W. Chen, Y. Yamamoto, W.H. Peter, M.B. Clark, S.D. Nunn, J.O. Kiggans, T. R. Muth, C.A. Blue, J.C. Williams, K. Akhtar, The investigation of die-pressing and sintering behavior of ITP CP-Ti and Ti-6Al-4 V powders, J. Alloys Compd. 541 (2012) 440–447, https://doi.org/10.1016/j.jallcom.2012.06.131.

[34] Q. Yan, B. Chen, N. Kang, X. Lin, S. Lv, K. Kondoh, S. Li, J.S. Li, Comparison study on microstructure and mechanical properties of Ti-6Al-4 V alloys fabricated by powder-based selective-laser-melting and sintering methods, Mater. Charact. 164 (2020), https://doi.org/10.1016/j.matchar.2020.110358.

[35] S. Dong, G. Ma, P. Lei, T. Cheng, D. Savvakin, O. Ivasishin, Comparative study on the densification process of different titanium powders, Adv. Powd. Tech. 32 (2021) 2300–2310, https://doi.org/10.1016/j.apt.2021.05.009.

[36] S. Tammas-Williams, H. Zhao, F. Léonard, F. Derguti, I. Todd, P.B. Prangnell, XCT analysis of the influence of melt strategies on defect population in Ti-6Al-4 V components manufactured by Selective Electron Beam Melting, Mater. Charact. 102 (2015) 47–61, https://doi.org/10.1016/j.matchar.2015.02.008.

[37] N. Dang, L. Liu, J. Adrien, S. Cazottes, W. Xiao, C. Ma, L. Zhou, E. Maire, Crack nucleation and growth in α/β titanium alloy with lamellar microstructure under uniaxial tension: 3D X-ray tomography analysis, Mater. Sci. Eng. A 747 (2019) 154–160, https://doi.org/10.1016/j.msea.2019.01.065.

[38] P. Tarín, I. Alonso, A.G. Simón, J.M. Badía, N.M. Piris, Characterization of the α ↔ β transformations in a Ti-6Al-2Sn-4Zr-6Mo (wt.%) alloy, Mater. Sci. Eng. A 481–482 (2008) 559–561, https://doi.org/10.1016/j.msea.2006.12.193.

[39] O. Lame, D. Bellet, M. Di Michiel, D. Bouvard, In situ microtomography investigation of metal powder compacts during sintering, Nucl. Instrum. Methods Phys. Res. B 200 (2003) 287–294, https://doi.org/10.1016/S0168-583X(02)01690-7.

[40] O. Lame, D. Bellet, M. Di Michiel, D. Bouvard, Bulk observation of metal powder sintering by X-ray synchrotron microtomography, Acta Mater. 52 (2004) 977–984, https://doi.org/10.1016/j.actamat.2003.10.032.

[41] F. Xu, X.F. Hu, H. Miao, J.H. Zhao, In situ investigation of ceramic sintering by synchrotron radiation X-ray computed tomography, Opt. Lasers Eng. 48 (2010) 1082–1088, https://doi.org/10.1016/j.optlaseng.2009.12.012.

[42] A. Vagnon, J.P. Rivière, J.M. Missiaen, D. Bellet, M. Di Michiel, C. Josserond, D. Bouvard, 3D statistical analysis of a copper powder sintering observed in situ by synchrotron microtomography, Acta Mater. 56 (2008) 1084–1093, https://doi.org/10.1016/j.actamat.2007.11.008.

[43] S. Terzi, L. Salvo, M. Suery, A. Dahle, E. Boller, In situ microtomography investigation of microstructural evolution in Al-Cu alloys during holding in semi-solid state, Trans. Nonferrous Metal Soc. Chin. 20 (2010) s734–s738, https://doi.org/10.1016/S1003-6326(10)60572-9.

[44] R. Pederson, O. Babushkin, F. Skystedt, R. Warren, Use of high temperature X-ray diffractometry to study phase transitions and thermal expansion properties in Ti-6Al-4 V, Mater. Sci. Tech. 19 (2003) 1533–1538, https://doi.org/10.1179/026708303225008013.

[45] F.R. Kaschel, R.K. Vijayaraghavan, A. Shmeliov, E.K. McCarthy, M. Canavan, P. J. McNally, D.P. Dowling, V. Nicolosi, M. Celikin, Mechanism of stress relaxation and phase transformation in additively manufactured Ti-6Al-4 V via in situ high temperature XRD and TEM analyses, Acta Mater. 188 (2020) 720–732, https://doi.org/10.1016/j.actamat.2020.02.056.

[46] L. Yang, M. Wang, B. Liu, Y. Du, W. Liao, situ XRD study on the phase transformations of the gas-atomized Ti-22Al-25Nb powder, Mater. Lett. 277 (2020), 128378, https://doi.org/10.1016/j.matlet.2020.128378.

[47] F. Bruneseaux, E. Aeby-Gautier, G. Geandier, J. Da Costa Teixeira, B. Appolaire, P. Weisbecker, A. Mauro, In situ characterizations of phase transformations kinetics in the Ti17 titanium alloy by electrical resistivity and high temperature synchrotron X-ray diffraction, Mater. Sci. Eng. A 476 (2008) 60–68, https://doi.org/10.1016/j.msea.2007.04.072.

[48] B. Callegari, J.P. Oliveira, K. Aristizabal, R.S. Coelho, P.P. Brito, L. Wu, N. Schell, F. A. Soldera, F. Mücklich, H.C. Pinto, In-situ synchrotron radiation study of the aging response of Ti-6Al-4 V alloy with different starting microstructures, Mater. Charact. 165 (2020), https://doi.org/10.1016/j.matchar.2020.110400.

[49] J.W. Elmer, T.A. Palmer, S.S. Babu, E.D. Specht, In situ observations of lattice expansion and transformation rates of α and β phases in Ti-6Al-4 V, Mater. Sci. Eng. A 391 (2005) 104–113, https://doi.org/10.1016/j.msea.2004.08.084.

[50] Y. Meng, M. Villa, K.V. Dahl, T.L. Christiansen, M.A.J. Somers, Synchrotron X-ray diffraction investigation of the effect of cryogenic treatment on the microstructure of Ti-6Al-4 V, Appl. Surf. Sci. 502 (2020), https://doi.org/10.1016/j.apsusc.2019.144087.

[51] Q. Meng, H. Li, K. Wang, S. Guo, F. Wei, J. Qi, Y. Sui, B. Shen, X. Zhao, Situ Synchrotron X-ray Diffraction Investigations of the Nonlinear Deformation Behavior of a Low Modulus Β-Type Ti36Nb5Zr Alloy, Metals (Basel) 10 (2020) 1619, https://doi.org/10.3390/met10121619.

[52] M. Coffigniez, L. Gremillard, X. Boulnat, Sinter-Based Additive Manufacturing of Graded Porous Titanium Scaffolds by Multi-Inks 3D Extrusion, Adv. Eng. Mater. (2022), https://doi.org/10.1002/adem.202201159.

[53] PyHST2, Software, (n.d.). https://software.pan-data.eu/software/74/pyhst2.

[54] J. Schindelin, I. Arganda-Carreras, E. Frise, V. Kaynig, M. Longair, T. Pietzsch, S. Preibisch, C. Rueden, S. Saalfeld, B. Schmid, J.Y. Tinevez, D.J. White, V. Hartenstein, K. Eliceiri, P. Tomancak, A. Cardona, Fiji: An open-source platform for biological-image analysis, Nat. Methods 9 (2012) 676–682, https://doi.org/10.1038/nmeth.2019.

[55] T.W. Ridler, S. Calvard, Picture Thresholding Using An Interactive Selection Method, in: IEEE Trans Syst Man Cybern smc-8, 1978, pp. 630–632.

[56] R. Dougherty, K.-H. Kunzelmann, Computing Local Thickness of 3D Structures with ImageJ, Microsc. Microanal. 13 (2007) 1678–1679, https://doi.org/10.1017/s1431927607074430.

[57] M. Newville, R. Otten, A. Nelson, A. Ingargiola, T. Stensitzki, Lmfit: non-linear least-square minimization and curve-fitting for Python, Zenodo (2021), https://doi.org/10.5281/zenodo.5570790.

[58] M. Coffigniez, Additive Manufacturing of 3D Architectured Metallic Biomaterials By Robocasting, INSA Lyon, 2021.

[59] P. Moghimian, T. Poiri, M. Habibnejad-korayem, J. Arreguin, J. Kroeger, Metal powders in additive manufacturing : A review on reusability and recyclability of common titanium, Nick. Alumin. Alloy 43 (2021), https://doi.org/10.1016/j.addma.2021.102017.

[60] A.G. Illarionov, F.V. Vodolazskiy, N.A. Barannikova, Y.I. Kosmatskiy, Y. V. Khudorozhkova, Influence of phase composition on thermal expansion of Ti-0.4Al, Ti-2.2Al-2.5Zr and Ti-3Al-2.5 V alloys, J. Alloys Compd. 857 (2021), 158049, https://doi.org/10.1016/j.jallcom.2020.158049.

[61] G.I. Nkou Bouala, N. Clavier, S. Martin, J. Léchelle, J. Favrichon, H.P. Brau, N. Dacheux, R. Podor, From in Situ HT-ESEM Observations to Simulation: How Does Polycrystallinity Affects the Sintering of CeO2 Microspheres? J. Phys. Chem. C 120 (2016) 386–395, https://doi.org/10.1021/acs.jpcc.5b10465.

[62] R.L. Penn, J.F. Banfield, Imperfect Oriented Attachment : Dislocation Generation in Defect-Free Nanocrystals, Science 281 (1998) 969–971, 1979.

[63] C. Baykasoglu, O. Akyildiz, D. Candemir, Q. Yang, A.C. To, Predicting Microstructure Evolution during Directed Energy Deposition Additive Manufacturing of Ti-6Al-4 V, J. Manuf. Sci. Eng. Trans. ASME 140 (2018), https://doi.org/10.1115/1.4038894.

[64] R.A. Perez, H. Nakajima, F. Dyment, Diffusion in α-Ti and Zr, Mater. Trans. 44 (2003) 2–13, https://doi.org/10.2320/matertrans.44.2.

[65] ThermoTech, TTTI3 Database, (n.d.). http://www.thermotech.co.uk/databases.html#Ti-DATA.